Shear-wave velocity structure and crustal lithology beneath the ultra-slow spreading Southwest Indian Ridge at 50°E

Xiongwei Niu[1,2], T. A. Minshull[3], Jiabiao Li[1,2]*, Aiguo Ruan[1,2]*, Zhenli Wu[1,2], Xiaodong Wei[1,2], Wei Wang[1,2], Yan Li[1,2], G. Bayrakci[3], Chongzhi Dong[1,2], Weiwei Ding[1,2], Yinxia Fang[1,2], Jie Zhang[1,2]

[1]Key Laboratory of Submarine Geosciences, Ministry of Natural Resources, Hangzhou 310012, China.

[2]Second Institute of Oceanography, Ministry of Natural Resources, Hangzhou 310012, China.

[3]School of Ocean and Earth Science, National Oceanography Centre Southampton, University of Southampton, Southampton, UK.

* Corresponding author: jbli@sio.org.cn, ruanag@sio.org.cn.

SUMMARY

Shear-wave velocities provide an important constraint on crustal lithology. Limited crustal shear wave data are available from the ultra-slow spreading mid-ocean ridges. We combine observations of both compressional (P) and shear (S) waves in ocean bottom seismometer data from the Southwest Indian Ridge to determine crustal P wave velocity (Vp), S wave velocity (Vs), Vp/Vs and Poisson’s ratio variations along the ridge at 49°17′E–50°49′E. Similar layered crustal structures were revealed beneath both the magmatically robust segment centers (Vp/Vs of 1.76–1.94, Poisson’s ratio of 0.26–0.32) and the non-transform discontinuity (NTD) between them (Vp/Vs of 1.76–2.03, Poisson’s ratio of 0.26–0.34). Because laboratory measurements show an overlap in Poisson’s ratio between mafic igneous rocks and ultramafic rocks, particularly at Vp values typical of oceanic Layer 3, it can be difficult to distinguish crustal composition using this parameter only. However, our observed Vp gradients of 0.1 ± 0.1 /s suggest that in this area, oceanic Layer 3 consists primarily of mafic igneous rocks both at segment centers and at the NTD. Oceanic crustal layers 2A and 2B above are likely also to consist of mafic igneous rocks, with some evidence for increased fracturing at the NTD.

Key words: crustal structure; mid-ocean ridge processes; composition and structure of the oceanic crust; controlled source seismology

1 INTRODUCTION

The oceanic crust is formed from basaltic melt generated by decompression melting of the mantle upwelling beneath mid-ocean ridges. The thickness and internal structure of this crust has been well characterized by wide-angle seismic profiles (e.g. Christeson *et al*. 2019; Grevemeyer *et al*., 2018; White *et al*. 1992). Typically a two-layer P-wave velocity structure is observed, with a high-gradient upper layer (Layer 2) underlain by a low-gradient lower layer (Layer 3). Based on a recent compilation (Christeson *et al*. 2019), for the young oceanic crust (age <7.5 Ma), the mean thicknesses of Layer 2 and 3 are 1.77 ± 0.60 km and 4.35 ± 1.09 km, respectively, resulting in a mean oceanic crust thickness of 6.12 ± 0.99 km. Layer 2 is commonly associated with extrusive basalts and sheeted dolerite dykes and Layer 3 is associated with gabbros (e.g. Cann 1974), though the seismic velocity is controlled by porosity as well as by lithology (e.g. Spudich & Orcutt, 1980).

However, oceanic crust formed by seafloor spreading at ultraslow rates of less than 20 mm yr^{-1}, such as at the Southwest Indian Ridge (SWIR) can be much thinner than 6 km thick (e.g. White *et al*. 2001; Minshull *et al*. 2006). In places, these ridges exhume serpentinised mantle to the seafloor (e.g. Sauter *et al*. 2004, 2013; Dick *et al*. 2003) and generate "amagmatic spreading segments" (Dick *et al.* 2003). In such locations the conventional layering of oceanic crust, with a distinct velocity discontinuity marking the base of mafic crust, may disappear completely. Instead, velocities may increase smoothly with depth as the degree of serpentinization decreases (e.g. Momoh *et al*. 2017), resulting in either a small velocity discontinuity at the base of the "crust" that marks a serpentinization front, or in no discontinuity at all. Elsewhere at such ridges, oceanic Layers 2 and 3 are observed (e.g. Minshull *et al*. 2006), but the exhumation of mantle rocks at both slow- and ultra-slow-spreading ridges has led some authors to question the association between Layer 3 and gabbros, with alternative models involving gabbroic intrusions within serpentinized mantle peridotite (e.g. Cannat 1993).

A good agreement between seismically determined crustal thicknesses (where P-wave velocities are less than 8 km/s) and igneous crustal thicknesses inferred from geochemical indicators of the degree of melting (e.g. White *et al*. 2001; Christeson *et al*. 2019) suggests that serpentinised peridotite may not be the dominant component in Layer 3 even at ultra-slow spreading ridges (e.g. Prada *et al*. 2016; Grevemeyer *et al*. 2018). At such ridges, velocity steps from <7.4 km/s at the bottom of Layer 3 to >7.9 km/s at the top of upper mantle are commonly observed (e.g. Christeson *et al*. 2019; Niu *et al*., 2015). Direct sampling of *in situ* Layer 3 rocks by deep drilling has proved elusive, but active source multi-component wide angle seismic studies can shed further insights into the petrological characteristics of the seismically defined oceanic crust at ultra-slow spreading ridges.

Based on P-wave velocities alone, it can be difficult to distinguish crustal lithologies, for example between mafic rocks and serpentinised ultramafics (e.g. Carlson & Miller 2003; Carlson 2018; Spudich & Orcutt 1980; White *et al.* 1992). Laboratory measurements (e.g. Christensen 1996) suggest that S-wave velocities provide a valuable additional constraint, and thus if both Vp and S-wave velocities (Vs) can be measured, lithologies within the oceanic lithosphere may be distinguished more effectively (e.g. Prada *et al*. 2016; Grevemeyer *et al*. 2018; Klingelhöfer *et al*. 2000; Peirce *et al*. 2020). The Vp/Vs ratio may be a useful proxy to distinguish mantle- and crustal-derived lithologies because both basalts and gabbros generally have Vp/Vs ratios of <1.9, while serpentinized mantle generally has much higher Vp/Vs ratios (e.g. Grevemeyer *et al*. 2018). However, compilations of laboratory measurements (e.g. Bayrakci *et al*. 2018) show that mafic igneous rocks can have overlapping Vp/Vs ratios. In this study, we use controlled source seismic data from two segments of the SWIR and the non-transform discontinuity (NTD) between them to determine the Poisson's ratio and Vp/Vs structure of the crust, and combine these with Vp gradients and other observations to draw inferences about crustal lithologies.

2 GEOLOGICAL SETTING

The SWIR is among the world's slowest-spreading ridges with an almost constant full spreading rate of ~14 mm/yr along the 7700 km ridge axis (Patriat *et al.* 1997). It extends from the Bouvet triple junction in the south Atlantic to the Rodriguez triple junction in the central Indian Ocean (Fig. 1). It trends obliquely to its north-south spreading direction and is offset northwards along several major north-south trending transform faults (e.g. Cannat *et al*. 1999). Our study area is located in the central shallow part of the SWIR (49.3°E to 50.8°E), which has a full spreading rate of 13.9 mm/yr (Mendel *et al*. 2003) and includes three axial volcanic ridge (AVR) segments (27 to 29; Fig. 1; Cannat *et al*. 1999; Mendel *et al*. 2003) with distinct topographies and two NTDs between them. Because of poor seismic sampling of segment 29 and the NTD between segments 28 and 29, in this study we focus only on segments 27 and 28 and the NTD between them. The Dragon Flag and Duan Qiao hydrothermal vents are located at segment 28 and segment 27, respectively (Tao *et al*., 2012; 2020).

Previous controlled source P-wave seismic studies in this area showed that: (1) The crust (above the Moho discontinuities (Moho) with Vp <7.0 km/s) beneath segment 27 is up to 10.5 km thick with a low-velocity zone (Niu *et al*. 2015; Li *et al*. 2015; Jian *et al*. 2017; Yu *et al*. 2018); (2) the adjacent segment 28 has thinner crust (7–8 km) with a detachment fault generated on its southern flank (Zhao *et al*. 2013; Niu *et al*. 2015; Yu *et al*. 2018); and (3) the ~18.5-km-long NTD between these segments has thinner crust (~5-6 km) (Zhao *et al*. 2013; Niu *et al*. 2015; Li *et al*. 2015; Yu *et al*. 2018). The thick crust inferred from seismic studies suggests that, in contrast to observations elsewhere on the SWIR, a rich magma supply may also occur at this ridge (Zhao *et al*. 2013; Niu *et al*. 2015; Li *et al*. 2015; Yu *et al*. 2018). Serpentinised peridotite outcrops have been observed and sampled around the west end of segment 28 (Tao *et al*. 2020).

3.DATA AND METHOD

During January-March 2010, a three-dimensional (3-D) controlled source four-component ocean-bottom seismometer (OBS) experiment was carried out by the R/V *Dayang Yihao* around SWIR segments 27 and 28 at 50°E. Four Bolt airguns with a total volume of 6000 in^3 (~100 L) were towed at a nominal depth of 10 m and fired at 120 s – 180 s intervals to give a nominal shot spacing of 200–300 m. This study focuses on one 138-km seismic profile with 12 OBSs along the ridge and spanning both segments (AB in Fig. 1). OBS spacings ranged from 4 km to 23 km. The OBS data (vertical and two horizontal geophone components) were corrected for clock drift, OBSs and shots were both relocated using direct arrivals, and data were band-pass filtered with a 4–20 Hz filter for P waves (Niu *et al*. 2015) and a 3–8 Hz filter for S waves. For S wave analysis, we rotated the two horizontal components into radial (in line) and transverse (cross-line) components using the orientation measured by a compass on the OBS or that determined by comparing the direct arrival energy for each trace at 1° intervals. For two-dimensional modelling, a straight-line approximation of the profile was determined by a least-squares fit to all the shots along the profile. The depth of each OBS was first estimated from multi-beam bathymetric data, and then refined by fitting the direct water wave arrivals (Pw).

In general, both the vertical and radial components of the seismic data are of sufficient quality to pick both crustal and mantle P and S arrivals, respectively, though S arrival pick uncertainties can be large due to the low signal-to-noise ratio (SNR) and their non-impulsive nature (Figs 2-3). We identified the Pw, P and S waves refracted from the oceanic crust and the upper mantle, denoted Pg, Pn and PSSg, PSSn, respectively, and P and S waves reflected from the Moho, denoted PmP and PSSmS, respectively. All the S phases were identified as PSS arrivals, which were converted from P to S at the seabed on the way down (Christensen 1996).

P-wave picks were guided by those of Niu *et al*. (2015), but they were re-picked (Table 1, Figs S1-S13 for details) to remove inconsistencies between picks from the vertical and radial components. Using both sets of picks effectively double-weights shot-receiver pairs where both are made, but given the high noise level of the dataset, this approach is justified by the resulting increased confidence in those picks compared to those from a single component only. We also increased the pick uncertainties for arrivals with very low SNR, to make sure there is an overlap of the error bars between the picked arrival times from the different components (Fig. S1b). In addition, analysis of radial component arrivals led us to add further PmP and Pn picks to achieve overall consistency (Fig. S1a). The Pg arrivals can be identified in both vertical and radial components at offsets of ~5–50 km (Figs 2-3) in all the OBSs except OBS 11, where we used hydrophone data (Niu *et al*. 2015). High-amplitude PmP arrivals were picked at ~11–55 km offset (Figs 2-3, S4, S7-S13) in the vertical data from eight OBSs (4, 21, 22, 23, 24, 25, 26 and 30) and in the radial data from five OBSs (4, 21, 22, 23, and 26). Pn was picked at offsets of over 20 km (Figs 2-3, S3-S10, S13) in both the vertical and radial data from nine OBSs (2, 4, 8, 11, 21, 22, 23, 24 and 30).

PSSg was picked in both vertical and radial data from most OBSs at offsets of ~5–50 km (Figs 2-3), except for the vertical data from four OBSs (2, 11, 16 and 21) and the radial data from OBS 16. PSSmS was picked at offsets of ~11–55 km in the vertical data from five OBSs (22, 24, 25, 26, and 30) and in the radial data from eight OBSs (4, 21, 22, 23, 24, 25, 26 and 30). Finally, low-amplitude PSSn arrivals were picked at offsets of over 30 km in the vertical data from two OBSs (22 and 24) and in the radial data from two OBSs (22 and 23). For picking uncertainties of S arrivals, we first picked S arrivals for each instrument, and then re-picked them. We assigned an uncertainty for each phase that was based on the difference between the two picks. We calculated the mean arrival time of the two picks as S wave arrivals. Since the SNR tends to decrease with increasing offset (Zelt & Smith 1992; Zelt & Forsyth 1994), for the noisier OBSs we also added an offset-dependent term, increasing the uncertainty by 1 ms per km of offset.

A total of 7859 P-wave and 2831 S-wave travel times were picked from the vertical and radial components of the 12 OBSs (Table 1). The final Vp crustal structure was obtained using the inversion and ray-tracing algorithms of Zelt & Smith (1992). This approach involves layered models in which the vertical velocity gradient within layers is invariant with depth. Our model included five layers: water layer, oceanic Layer 2A, oceanic Layer 2B, oceanic Layer 3 and the upper mantle. The velocity node spacings were 5–10 km, 5–10 km, 10–28 km and 20 km in Layers 2A, 2B, 3 and the mantle, respectively (Niu *et al.*, 2015). We fixed the velocity at the top of Layer 3 to be the same as the velocity at the bottom of Layer 2. Once we had obtained a final Vp model, we fitted the S wave data by adjusting the Poisson's ratios (Zelt & Smith 1992). Poisson's ratio was initially 0.50 in the water and 0.27 elsewhere. Then this parameter was changed in steps of 0.01 to fit the S wave data (e.g. Christensen 1996). We applied two criteria: (1) fitting as many picks as possible; and (2) obtaining a $\chi2$ value as close as possible to 1.0. We selected a model with $\chi2 = 1.201$ and 2765 (97.7%) fitted picks as the final model. The Vs model was then calculated based on the Vp and Poisson's ratio models.

For each velocity node, we used the velocity at the bottom of the layer (V_{pb}), the velocity at the top of the layer (V_{pt}) and the layer thickness of H to determine the velocity gradient $V_{pG} = (V_{pb} - V_{pt})/H$. Mean velocity gradients were calculated using the mean Vp at the top and bottom of the layer and the mean layer thickness.

4 RESULTS

4.1 New P-wave velocity model and comparison with previous model

Niu *et al*. (2015) needed two different Moho depths in the western part of their model (Moho and alternative Moho shown at depth of 8–10 km and distance of 14–75 km in Fig. 8 of Niu *et al*. 2015 and Figs S2-S13) to fit their PmP picks from all OBSs, attributing this requirement to off-line three-dimensional effects. Using our more extensive picking of PmP and Pn that uses both the vertical and radial components (Fig. S1c), and informed by the two models of Niu *et al*. (2015) and the 3D model of Zhao *et al*. (2013), we were able to resolve this ambiguity. The ambiguity arises from a trade-off between depth and velocity when modelling the PmP phase, due to a lack of turning waves in the lower crust. Ultimately we found a single velocity model that fits both sets of picks from all OBSs. The resulting model uses more picks and has smaller misfit and smaller χ^2 than that of Niu *et al*. (2015, Figs. S2-S13). The main change in the model from the preferred model of Niu *et al*. (2015) is the distribution of Moho reflection points beneath Segment 28 and the adjacent NTD (Figs. S14-S15). The Moho depth beneath Segment 28 differs significantly from the preferred model of Niu *et al*. (2015) but fits well the PmP arrivals (Tables 1 and 2, Fig. S1c) and matches well both their alternative model (Fig. S14-S15) and the 3D model of Zhao *et al*. (2013), which is sampled in Fig. 11 of Niu *et al*. (2015). The fit to gravity data is not improved (Fig. S16), but misfits can be readily attributed to structure out of the plane of the profile. The other differences from the models of Niu *et al*. (2015) are as follows: (1) there are lower velocities at the top of the upper mantle beneath the NTD; (2) there is less lateral velocity variation in Layers 2A and 2B; and (3) the velocity at the top of Layer 3 is 6.2 km/s, compared with 6.4 km/s in the previous model. The root-mean-square (RMS) velocity difference between this model and the two models of Niu *et al*. (2015) is no more than 0.1 km/s, which is not higher than the velocity uncertainties of our new model (Table 3).

The new Vp model shows that segments 27 and 28 have similar velocity structures in Layers 2A (0.5–1.0 km thickness), 2B (~2.0 km thick) and 3 (6.0–8.0 km thick) (Fig. 4a). Some along-axis velocity variations occur in Layers 2A and 2B, with velocities about 1.0 km/s higher in segment centers, while no along-axis variations were required in Layer 3. The velocity at the top of the upper mantle beneath both segments is 8.0 km/s. We calculate Vp gradients within each layer (Table 4). The mean Vp gradients in Layers 2A, 2B and 3 are 1.7 s^{-1}, 1.2 s^{-1} and 0.1 s^{-1}, respectively.

Beneath the NTD, the same three-layer structure is present. The thickness of Layer 2A is about 0.2–0.7 km, which is thinner than in the adjacent magmatic segments. Layer 2B shows the same thickness as in the adjacent segments (about 2 km), while Layer 3 (about 4–5 km thick) is significantly thinner than in the adjacent segments. In the NTD, the top of Layer 2B shows a lower velocity (4.0 km/s), as does the top of the upper mantle (7.7 km/s).

4.2 S-wave velocity model

We show S-wave velocities along with Vp/Vs ratios and Poisson's ratio (Fig. 4b-d). The PSSmS phase is well fit by the new Moho geometry (Figs 2-3). There is little along-axis velocity variation in Layer 2A with velocities around 1.3 km/s, while larger along-axis velocity variations occur at the top of Layer 2B between the magmatic segments (~2.8 km/s) and the NTD (~2.2 km/s). Velocities in Layer 3 beneath the magmatic segments show little along-axis variation, increasing with depth (from 3.6 km/s at the top to 4.0 km/s at the bottom with velocity gradients of ~0.1 s^{-1} beneath segment 28 and segment 27). Layer 3 velocities are lower at the NTD (from 3.5 km/s at the top to 3.9 km/s at the bottom with a velocity gradient of ~0.1 s^{-1}). Because of the lack of PSSn data, we can only constrain Vs at the top of the upper mantle beneath segment 28 (4.6 km/s) and beneath the NTD (4.4 km/s).

A large Vs discontinuity is present between the bottom of Layer 2B and the top of Layer 3 (Fig. 4). This discontinuity arises because Poisson's ratio in the model cannot change with depth within a layer. In reality, Poisson's ratio probably decreases with depth, so this discontinuity is likely an artifact of model parameterisation and Vs may be over-estimated at the top of Layer 3 and under-estimated at its base.

4.3 Error analysis and uncertainty

The overall χ^2 value for our P-wave model was 1.061, with 95.6% of the picks fitted. The overall RMS misfit for the Vp model was 132 ms. For the S-wave picks on both components, the overall RMS misfit was 187 ms and the overall χ^2 value was 1.201, with 97.7% of the picks fitted. These values suggest that the model was suitably parameterised, with a final travel-time misfit slightly larger than the pick uncertainty. In order to calculate the ray density, following Zelt & Smith (1992), we interpolated the model onto 0.25 × 0.25 km cells. The number of rays through each cell was generally larger than 10 and reached over 100 (Fig. S17), indicating that the model is well constrained except near the ends. Because there may be a trade-off for the wide-angle reflections (i.e., PmP), we estimated Moho depth uncertainties by using the F-test to determine the size of the perturbation required to give a statistically different misfit (Zelt & Smith 1992). Crustal velocity and Poisson's ratio uncertainties were also estimated using the F-test (Table 3). Velocity uncertainties in all the layers are shown to be less than 0.4 km/s (Table 3). Poisson's ratio uncertainties in Layers 2A and 2B are slightly larger, ranging from -0.04 to 0.03 and -0.01 to 0.03, respectively, while they are very small in Layer 3 and the upper mantle, ranging from -0.01 to 0.01 (Table 3).

Along the 138 km profile, ~90 km of Moho was controlled by 955 PmP arrivals (Fig 4a), ~65 km of Moho was controlled by 655 PSSmS arrivals (Fig 4b). We tested the trade-off between the Moho depth and the bottom velocity of Layer 3, yielding a maximum of -1.0 km to +0.8 km Moho depth uncertainty when the bottom velocity of Layer 3 is varied between its confidence limits at 0.1 km/s increments (Table 5). Each time we changed the bottom velocity of Layer 3, we use the F-test to test the depth uncertainty of Moho (Zelt & Smith 1992), varying Moho depth by 0.1 km increments until the 97% confidence limit is reached. The quoted uncertainty spans the maximum and minimum Moho depth lying within this limit across all the sampled velocities. We also used the F-test to estimate the uncertainty of the Vp gradient in each layer, by perturbing the top and bottom Vp in increments of 0.1 km/s, while keeping the mean Vp constant and the velocity gradient non-negative.

5 DISCUSSION

The seismic crustal thickness varies from ~8.0 km beneath Segment 28 to ~6.3 km beneath the NTD and ~10.0 km beneath Segment 27 (Figs 4a, 4b). Thick crust is beneath the AVRs but there is reduced crustal thickness beneath the NTD, as observed elsewhere on the Southwest Indian Ridge (e.g. Minshull *et al*. 2006; Muller *et al*. 2000).

5.1 Petrological characteristics of Layer 2 and Layer 3

In order to examine the petrological character of the crust in our study area, we compared our P-wave velocity structure with 0-7.5 Ma crust at slow-spreading ridges with half spreading rates of 5-20 mm/year (Christeson *et al*. 2019), and Vp/Vs and Poisson's ratio structures with the ultraslow-spreading Mid-Cayman Spreading Centre (Grevemeyer *et al*. 2018) and Mohns ridge (Klingelhöfer *et al*. 2000).

As noted by Grevemeyer *et al.* (2018), both basalts and gabbros generally have Vp/Vs of <1.9, while serpentinised mantle commonly has higher values, though they can range from ~1.8 (for very low degrees of alteration) to >2.1. Based on the classification approach of Grevemeyer *et al*. (2018), Layers 2A and 2B in our study area beneath the segment centers and NTD, with a Vp/Vs of >1.9 could be composed of serpentinite with high degrees of alteration. The Poisson's ratio of >0.3 in Layers 2A and 2B may also represent serpentinites (Fig. 5c). Based on compilations of laboratory data (e.g. Bayrakci *et al*. 2018), Layers 2A and 2B in our profile have values more consistent with mafic rocks, though part of Layer 2B has values that are also consistent with ultramafic rocks

(Fig. 5d).

Layer 3 in our model has Vp/Vs and Poisson's ratio values that lie in the basalt and gabbro fields of Grevemeyer *et al*. (2018) (Fig. 5c), but span the mafic and ultramafic fields defined by laboratory measurements (Bayrakci *et al*. 2018; Fig. 5d). Thus Vp/Vs is not always useful for distinguishing the mafic rock and serpentinite. Klingelhöfer *et al*. (2000) also pointed out that, based on S-and P-wave modelling of data from zero-age crust at Mohns Ridge (Fig. 5c), it was not possible to distinguish between 100 per cent gabbro or 10-40 per cent serpentinised peridotite.

The Vp gradients may tell a different story (Table 4, Fig. 6). The Vp gradient of a gabbroic Layer 3 is normally <0.2 s^{-1} (e.g. Carlson 2018; Spudich & Orcutt 1980; Christeson *et al*. 2019), but Vp gradients in serpentinite are likely to fall in a range 0.6–2.1 /s, based on a velocity increase from 5.0 to 8.0 km/s in a serpentinite layer thickness of 2-5 km (e.g. Minshull 2009). Thus, Layer 3 in our profile, with Vp gradients of 0.1±0.1 /s that are significantly lower than that observed at Mohns Ridge (Table 4, Fig. 6), is more likely to consist of gabbro than serpentinite (Fig. 6).

Layer 3 beneath segments 27 and 28 has a Vp that is lower than that of <7.5 Ma crust at ridges with half spreading rates of 5–20 mm/year (Christeson *et al*. 2019, Fig. 5a). A low-velocity zone (LVZ) with a Vp reduction of ~0.6 km/s is also revealed by previous P wave studies at segment 27 (Li *et al*. 2015; Jian *et al*. 2017). The LVZ may result from high temperatures and/or a small amount of melt (Jian *et al*. 2017). The reduced velocities that we observe are consistent with the presence of such a zone, but we cannot resolve it in a layered Vp model with vertically invariant gradients. Using effective medium theory, Jian *et al*. (2017) showed that this LVZ can be explained by the presence of at least 3–10% melt inclusions in its upper part. The presence of melt reduces both Vp and Vs and increases the Poisson's ratio (Fig. 5c). The low Poisson's ratio that we observe suggests that melt volumes are insufficient to influence this value at the resolution of our model.

If Layer 3 is gabbroic, it is very unlikely that Layer 2 is serpentinite because one would expect to see some extrusives and dykes above the gabbros (e.g. Christeson *et al*. 2019). Moreover, the predominance of basalt in dredge samples (Zhou & Dick 2013), which likely sample a range of stratigraphic levels, favours a basaltic composition throughout. As a result, although the Layer 2 Vp/Vs, Poisson's ratio and Vp gradient could be consistent with either mafic or ultramafic composition, the gabbroic Layer 3 and the dredge samples at the seabed suggest a mafic composition for Layer 2 in our study area.

5.2 Crustal petrological characteristics beneath the NTD and segment centers

Although crustal thickness is similar, there are some differences between the NTD and segments 27 and 28 in Layer 2B. The high Vp gradient, low Vs, high Vp/Vs and high Poisson's ratio values beneath the NTD (Table 4, Figs 4, 5b) suggest that the crust there is more fractured than beneath the magmatic segments, which have lower Vp gradient, higher Vs, lower Vp/Vs and lower Poisson's ratio (e.g. Grevemeyer *et al*. 2018; Christeson *et al*. 2019).

Vp/Vs ratios and Poisson's ratio in Layer 3 beneath the NTD are also higher than those beneath segments 27 and 28 (Fig. 5b). Previous geophysical and geochemical studies of NTDs at ultra-slow spreading ridges have suggested that oceanic Layer 3 may be missing in these regions (e.g. Minshull *et al*. 2006; Zhou & Dick 2013). Furthermore, the presence of a thick crust (>6 km) beneath both the NTD and segment centers around SWIR 50°E indicates that a mafic composition is more likely (e.g. Minshull *et al*. 1998), and the simplest explanation for the differences in Layer 3 velocities between the NTD and segment centers is that the lithologies present are similar. Vp gradients in Layer 3 beneath the NTD and segment centers are quite similar and both in the range of typical oceanic crust (Table 4, Fig. 6, Christeson *et al*. 2019; Spudich & Orcutt 1980; White *et al*. 1992). Clearly high-amplitude PmP reflections can generated at the Moho beneath the NTD, similar to those beneath the segment centers (Figs. 3), representing a strong velocity contrast between the bottom of Layer 3 and the top of upper mantle (e.g. Minshull *et al*., 2006). Hence, in our preferred interpretation, Layer 2 is more fractured and Layer 3 is thinner beneath the NTD, but the crustal composition is similar.

5.3 Petrological characteristics of Moho

Moho as the basement of the crust may be interpreted as either a serpentinization front or a petrological boundary between mafic rocks above and ultramafic rocks below (e.g. Minshull 2009). One of the key information to distinguish them is the wide-angle reflections. Previous studies have reported that a large number of wide-angle reflections from the Moho represent a sharp boundary as the bottom of the normal oceanic crust, and absent Moho reflections may represent a serpentinization front or transition zone. (e.g. Simão *et al*. 2020; Minshull 2009; Minshull *et al*. 1998; Hess 1962). Another method to distinguish them is the Moho depth. As summarized by Minshull (2009), for where there is no large deep fault, the deepest depth for the sea water to reach is ~5 km, which means the serpentinization front may not occur at the Moho at depth below seabed greater than 5 km. Fig. 4 shows the Moho in our Vp and Vs models were not only adequately controlled by PmP and PSSmS, which almost cover the whole parts of segments 27 and 28 and the NTD between them, but also at depth greater than ~6.5 km. Hence the Moho in our study area may reflect a sharp boundary rather than a serpentinization front. This interpretation is also consistent with our Vp structures of 7.0 km/s at the bottom of Layer 3 and 7.7~8.0 km/s at the top of upper mantle. As mentioned above, if Layers 2 and 3 are composed of mafic rocks, Moho is reasonable as a sharp boundary between mafic and ultramafic rocks in our study area.

6 CONCLUSIONS

Travel-time modeling of wide-angle seismic Vp and Vs data from OBSs deployed along the axis on the ultra-slow spreading Southwest Indian Ridge around 50°E led to the following conclusions.

(1) Beneath magmatic segments 27 and 28, Vs in crustal layers 2A, 2B and 3 is 1.0–1.6, 2.5–3.3 and 3.6–4.0 km/s, respectively. Beneath the non-transform discontinuity (NTD) between the segments, Layers 2A, 2B and 3 remain well-defined and have Vs values of 1.3–1.7, 2.2–3.2, and 3.5–3.9 km/s, respectively.

(2) Along the ridge, oceanic Layers 2A and 2B are basaltic, but beneath the NTD these rocks are more fractured than beneath segments 27 and 28.

(3) Although our calculated Vp/Vs and Poisson’s ratios do not lead to a unique

interpretation of lithology, Vp gradients of 0.1±0.1 /s suggest that gabbro dominates Layer 3 in our study area.

DATA AVAILABILITY

The seismic data used in this study are available by contacting the corresponding authors.

ACKNOWLEDGEMENTS

We are grateful to the scientists and crew of the of the R/V *DayangYihao* on Leg 6 of cruise DY115-21. This research is supported by the National Natural Science Foundation of China (grants 41876060, 42076047, 41890811 and 91858214). We used the RayInvr code (Zelt & Smith 1992) for seismic inversion. Some of our figures were plotted using GMT (Wessel & Smith 1998). We thank Professors D. Sauter, J. C. Sibuet, M. H. Zhao and Chuanwan Dong and Dr. Wei Li for the discussions. The data analysis was completed during a visit by X.N. to the National Oceanography Centre Southampton, University of Southampton. T. M. was partially supported by a Wolfson Research Fellowship. We thank Manel Prada and an anonymous reviewer, and editor Jenny Collier, for constructive comments that improved the manuscript.

References:

Bayrakci, G., Falcon-Suarez, I. H., Minshull, T. A., North, L., Barker, A., Zihlmann, B., Roumejon S., & Best, A. I., 2018. Anisotropic physical properties of mafic and ultramafic rocks from an oceanic core complex. *Geochemistry, Geophysics, Geosystems*, **19**, 4366–4384. https://doi.org/10.1029/2018GC007738

Blackman, D. K., Ildefonse, B., John, B. E., Ohara, Y., Miller, D. J., MacLeod, C. J., & Scientists, A. T. E., 2006. Oceanic core complex formation, Atlantis Massif. *Proceedings of the Ocean Drilling Program*, **304/305**. https://doi.org/10.2204/iodp.proc.304305.2006

Cann, J. R., 1974. A model for oceanic crustal structure developed. *Geophysical Journal of the Royal Astronomical Society*, **39**, 169-187.

Cannat, M., 1993. Emplacement of mantle rocks in the seafloor at mid-ocean ridges, *Journal of Geophysical Research*, **98**, 4163-4172.

Cannat, M., Rommevaux-Jestin, C., Sauter, D., Deplus, C., & Mendel, V., 1999. Formation of the axial relief at the very slow spreading Southwest Indian Ridge (49° to 69°E). *Journal of Geophysical Research: Solid Earth*, **104**(B10), 22825–22843. https://doi.org/10.1029/1999JB900195

Carlson, R. L., 2018., Ocean crustal seismic layer 2C. *Geochemistry, Geophysics, Geosystems*, **19**, 3084–3096. https://doi.org/10.1029/ 2018GC007614

Carlson, R. L., & Miller, D. J., 2003. Mantle wedge water contents estimated from seismic velocities in partially serpentinized peridotites, *Geophysical Research Letters*, **30**(5), 1250. https://doi.org/10.1029/2002GL016600

Christensen, N. I., 1996. Poisson’s ratio and crustal seismology. *Journal of Geophysical Research: Solid Earth*, **101**(B2), 3139–3156. https://doi.org/10.1029/95JB03446

Christensen, N. I., 1966. Elasticity of ultrabasic rocks. *Journal of Geophysical Research*, **71**, 5921–5931. https://doi.org/10.1029/JZ071i024p05921

Christeson, G. L., Goff, J. A., & Reece, R. S., 2019. Synthesis of oceanic crustal structure from two‐dimensional seismic profiles. *Reviews of Geophysics*, **57**, 504–529. https://doi.org/10.1029/2019RG000641

Dick, H. J. B., Lin, J., & Schouten, H., 2003. An ultraslow-spreading class of ocean ridge. *Nature*, **426**(6965), 405–412. https://doi.org/10.1038/nature02128

Früh-Green, G. L., Orcutt, B. N., Green, S., Cotterill, C., & the Expedition 357 Scientists., 2017. Expedition 357 summary. *Proceedings of the International Ocean Discovery Program*, Expedition Reports 357. https://doi.org/10.14379/iodp.proc.357.101.2017

Grevemeyer, I., Hayman, N. W., Peirce, C., Schwardt, M., van Avendonk, H. J. A., Dannowski, A., & Papenberg, C., 2018. Episodic magmatism and serpentinized mantle exhumation at an ultraslow-spreading centre. *Nature Geoscience*, **11**, 1–5. https://doi.org/10.1038/s41561-018-0124-6

Hess, H. H., 1962. History of the ocean basins. In: Engel, A. E., James, H. L., and

Leonard, B. F., *Petrologic Studies*, Burlington Volume. Geological Society of America, Boulder, Colorado, 599-620.

Iturrino, G. J., Miller, D. J., & Christensen, N. I., 1996. Velocity behavior of lower crustal and upper mantle rocks from a fast-spreading ridge at hess deep. In *Proceedings of the Ocean Drilling Program*, Scientific Results. **147**, 417–440. College Station, TX: Ocean Drilling Program

Iturrino, G. J., Christensen, N. I., Kirby, S. H., & Salisbury, M. H., 1991. Seismic velocities and elastic properties of oceanic gabbroic rocks from Hole 735B. In: Von Herzen, RP; Robinson, PT; et al. (eds.), *Proceedings of the Ocean Drilling Program, Scientific Results*, **118**, 227-244. College Station, TX: Ocean Drilling Program. https://doi.org/10.2973/odp.proc.sr.118.151.1991

Jian, H., Singh, S. C., Chen, Y. J., & Li, J., 2017. Evidence of an axial magma chamber beneath the ultraslowspreading Southwest Indian Ridge. *Geology*, **45**(2), 143–146. https://doi.org/10.1130/G38356.1

Klingelhöfer, F., Géli, L., Matias, L., Steinsland, N., & Mohr, J., 2000. Crustal structure of a super-slow spreading centre: A seismic refraction study of Mohns Ridge, 72°N. *Geophysical Journal International*, **141**(2), 509–526. https://doi.org/10.1046/j.1365-246X.2000.00098.x

Li, J., Jian, H., Chen, Y. J., Singh, S. C., Ruan, A., Qiu, X., Zhao, M., Wang, X., Niu, X., Ni, J., & Zhang, J., 2015. Seismic observation of an extremely magmatic accretion at the ultraslow spreading Southwest Indian Ridge. *Geophysical Research Letters*, **42**, 1–8. https://doi.org/10.1002/2014GL062521

Mendel, V., Sauter, D., Rommevaux-Jestin, C., Patriat, P., Lefebvre, F., & Parson, L. M., 2003. Magmato-tectonic cyclicity at the ultra-slow spreading Southwest Indian Ridge: Evidence from variations of axial volcanic ridge morphology and abyssal hills pattern. *Geochemistry, Geophysics, Geosystems*, **4**(5), 1–23. https://doi.org/10.1029/2002GC000417

Minshull, T. A., 2009. Geophysical characterisation of ocean-continent transition at magma-poor rifted margins. *Oceanography.* **341**, 382 – 393. http://dx.doi.org/10. 1016/j.crte.2008.09.003.

Minshull, T. A., Muller, M. R., Robinson, C. J., White, R. S., & Bickle, M. J., 1998. Is the oceanic Moho a serpentinization front? *Geological Society, London, Special Publications*, **148**(1), 71–80. https://doi.org/10.1144/GSL.SP.1998.148.01.05

Minshull, T. A., Muller, M. R., & White, R. S., 2006. Crustal structure of the Southwest Indian Ridge at 66°E: Seismic constraints. *Geophysical Journal International*, **166**(1), 135–147. https://doi.org/10.1111/j.1365-246X.2006.03001.x

Muller, M. R., Minshull,T.A., & White, R. S., 2000. Transient calculation of pressure waves in a well induced by tubular expansion. *Journal of Geophysical Research*, **105**(B11), 25809–25828. https://doi.org/10.1016/j.proeng.2017.09.281

Miller, D. J. & Christensen, N. I., 1997. Seismic velocities of lower crustal and upper mantle rocks from the slow-spreading Mid-Atlantic Ridge, south of the Kane Transform Zone (MARK). In J. A. Karson, M. Cannat, D. J. Miller, D. Elthon (Eds.), In *Proceedings of the Ocean Drilling Program*, Scientific Results. **153**. 437–454. College Station, TX: Ocean drilling Program. https://doi.org/10.2973/odp.proc.sr.153.043.1997

Momoh, E., Cannat, M., Watremez, L., Leroy, S. & Singh, S. C., 2017. Quasi-3-D Seismic Reflection Imaging and Wide-Angle Velocity Structure of Nearly Amagmatic Oceanic Lithosphere at the Ultraslow-Spreading Southwest Indian Ridge, *J. Geophys. Res. Solid Earth,* 122, 9511-9533. https://doi.org/10.1002/2017jb014754.

Niu, X., Ruan, A., Li, J., Minshull, T. A., Sauter, D., Wu, Z., Qiu, X., Zhao, M., Chen, Y. J., & Singh. S., 2015. Along-axis variation in crustal thickness at the ultraslow spreading Southwest Indian Ridge (50?E) from a wide-angle seismic experiment. *Geochemistry, Geophysics, Geosystems*, **16**, 468–485. https://doi.org/10.1002/2014GC005645

Patriat, P., Sauter, D., Munschy M., & Parson L. M., 1997. A survey of the Southwest Indian Ridge axis between Atlantis II Fracture Zone and the Indian Triple Junction: Regional setting and large scale segmentation, *Marine Geophysical Research*, **19**, 457–480.

Peirce, C., Robinson, A.H., Funnell, M.J., Searle, R.C., MacLeod, C.J., & Reston T.J., 2020. Magmatism versus serpentinization—crustal structure along the 13°N segment at the Mid-Atlantic Ridge. *Geophysical Journal International*, **221**, 981–1001.

Prada, M., Ranero, C. R., Sallarès, V., Zitellini, N., & Grevemeyer, I., 2016. Mantle exhumation and sequence of magmatic events in the Magnaghi–Vavilov Basin (Central Tyrrhenian, Italy): New constraints from geological and geophysical observations. *Tectonophysics*, **689**, 133–142. doi:10.1016/j.tecto.2016.01.041

Sauter, D., Patriat, P., Rommevaux-Jestin, C., Cannat, M., Briais, A., & Gallieni Shipboard Scientific Party., 2001. The Southwest Indian Ridge between 49º15’E and 57ºE: Focused accretion and magma redistribution: evidence for along-axis magma distribution. *Earth and Planetary Science Letters*, **192**(3), 303–317. https://doi.org/10.1016/S0012-821X(01)00455-1

Sauter, D., Cannat, M., Meyzen, C., Bezos, A., Patriat, P., Humler, E., & Debayle, E., 2009. Propagation of a melting anomaly along the ultraslow Southwest Indian Ridge between 46°E and 52°20′E: Interaction with the Crozet hotspot?

Geophysical Journal International, **179**(2), 687–699. https://doi.org/10.1111/j.1365-246X.2009.04308.x

Sauter, D., Carton, H., Mendel, V., Munschy, M., Rommevaux-Jestin, C., Schott, J. J., & Whitechurch, H., 2004. Ridge segmentation and the magnetic structure of the Southwest Indian Ridge (at 50°30′E, 55°30′E and 66°20′E): Implications for magmatic processes at ultraslow-spreading centers. *Geochemistry, Geophysics, Geosystems*, **5**(5). https://doi.org/10.1029/2003GC000581

Sauter, D., Cannat M., Rouméjon S., Andreani M., Birot D., Bronner A., Brunelli D., Carlut J., Delacour A., Guyader V., MacLeod C. J., Manatschal G., Mendel V., Ménez B., Pasini V., Ruellan E., & Searle R., 2013. Continuous exhumation of mantle-derived rocks at the Southwest Indian Ridge for 11 million years, *Nature Geoscience*, **6**, 314–320. doi:10.1038/ngeo1771

Simão, N.M., Peirce, C., Funnell, M.J., Robinson, A.H., Searle, R.C., MacLeod, C.J. & Reston, T.J., 2020, 3-D P-wave velocity structure of oceanic core complexes at 13°N on the Mid-Atlantic Ridge. *Geophysical Journal International*, **221**(3), 1555–1579.

Spudich, P., & Orcutt, J., 1980. A new look at the seismic velocity structure of the oceanic crust. *Reviews of Geophysics*, **18**(3), 627–645. https://doi.org/10.1029/RG018i003p00627

Tao, C., Lin, J., Guo, S., Chen, Y. J., Wu, G., Han, X., German, C. R., Yoerger, D., Zhou, N., Li, H., Su, X., Zhu, J., & the DY115-19 (Legs 1–2) and DY115-20 (Legs 4–7) Science Parties., 2012. First active hydrothermal vents on an ultraslow-spreading center: Southwest Indian Ridge. *Geology*, **40**(1), 47–50. https://doi.org/10.1130/G32389.1

Tao, C., Jr Seyfried, W. E., Lowell, R. P., Liu, Y., Liang, J., Guo, Z., Ding, K., Zhang H., Liu, J., Qiu, L., Egorov, I., Liao, S., Zhao, M., Zhou, J., Deng, X., Li, H., Wang, H., Cai, W., Zhang, G., Zhou, H., Lin, J., & Li, W. 2020. Deep high-temperature hydrothermal circulation in a detachment faulting system on the ultra-slow spreading ridge. *Nature Communications*, **11**(1300), 1-9. https://doi.org/10.1038/s41467-020-15062-w

Wessel, P. & Smith, W. H. F., 1998. New, improved version of generic mapping tools released. *Eos*, Transactions American Geophysical Union **79**(47), 579–579. https://doi.org/10.1029/98EO00426

White, R. S., McKenzie, D., & O'Nions, R. K., 1992. Oceanic crustal thickness from seismic measurements and rare earth element inversions. *Journal of Geophysical Research*, **97**(B13), 19683-19715. https://doi.org/10.1029/92JB01749

White, R. S., Minshull, T. A., Bickle, M. J. & Robinson, C. J., 2001. Melt generation at very slow-spreading oceanic ridges: constraints from geochemical and geophysical data, *J. Petrology*, **42**, 1171-1196.

Yu, Z., Li, J., Niu, X., Rawlinson, N., Ruan, A., Wang, W., Hu, H., Wei, X., Zhang, J., & Liang, Y., 2018. Lithospheric Structure and Tectonic Processes Constrained by Microearthquake Activity at the Central Ultraslow-Spreading Southwest Indian Ridge (49.2° to 50.8°E). *Journal of Geophysical Research: Solid Earth*, **123**(8), 6247–6262. https://doi.org/10.1029/2017JB015367

Zelt, C. A. & Smith, R. B., 1992. Seismic traveltime inversion for 2-D crustal velocity structure. *Geophysical Journal International*, **108**(1), 16–34. https://doi.org/10.1111/j.1365-246X.1992.tb00836.x

Zelt, C. A. & Forsyth, D. A., 1994. Modeling wide-angle seismic data for crustal structure: Southern Grenville Province. *Journal of Geophysical Research*, **99**(B6), 11687–11704. https://doi.org/10.1029/93JB02764

Zhao, M., Qiu, X., Li, J., Sauter, D., Ruan, A., Chen, J., Cannat, M., Singh, S., Zhang, J., Wu, Z., & Niu, X., 2013. Three-dimensional seismic structure of the Dragon Flag oceanic core complex at the ultraslow spreading Southwest Indian Ridge (49°39′E). *Geochemistry, Geophysics, Geosystems*, **14**(10), 4544–4563. https://doi.org/10.1002/ggge.20264

Zhou, H. Y. & Dick, H. J. B., 2013. Thin crust as evidence for depleted mantle supporting the Marion Rise, *Nature*, **494**, 196–201, doi: 10.1038/nature11842

Table 1. Statistics of Travel-time Analysis.

Phases	Total picks	Inverted Picks	Fit ratio (%)	Uncertainties (ms)	RMS (ms)	χ2	Picks / Uncertainties of Niu et al., 2015 (ms)
*Pw Vertical	211	211	100.0	50	36	0.514	316 / 30
Pw Radial	227	227	100.0	50	35	0.490	/
Pg Vertical	2617	2499	95.5	50-250	103	1.298	2034 / 50-73
Pg Radial	2134	2032	95.2	123-200	156	1.005	/
PmP Vertical	649	641	98.8	100-150	96	0.600	660 / 119-164
PmP Radial	314	314	100.0	131-156	155	1.169	/
Pn Vertical	1075	1025	95.3	73-250	147	1.017	770 / 100-188
Pn Radial	632	563	89.1	145-200	184	1.204	/
All P wave	**7859**	**7512**	**95.6**	**/**	**132**	**1.061**	**/**
PSSg Vertical	809	781	96.5	102-159	150	1.416	/
PSSg Radial	1201	1184	98.6	155-210	176	1.018	/
PSSmS Vertical	216	211	97.7	150-202	226	1.325	/
PSSmS Radial	458	444	96.9	192-235	258	1.486	/
PSSn Vertical	72	70	97.2	144-200	115	0.561	/
PSSn Radial	75	75	100.0	192-235	149	0.494	/
All S wave	**2831**	**2765**	**97.7**	**/**	**187**	**1.201**	**/**

Note: *When we projected the OBS to the 2-D profile, its depth was adjusted to the water depth at the 2-D profile, resulting a good consistent of Pw arrivals. The bold values and text are the summaries or average values of P wave data (lines 2–9) or S wave data (lines 11–16).

Table 2. Travel-time Analysis for the Moho discontinuity.

	Vertical component			Radial component		
	Segment 28	NTD	Segment 27	Segment 28	NTD	Segment 27
Number of picks	196	193	488	170	207	311
RMS (ms)	117	141	156	158	208	269
χ2	0.842	0.973	0.858	0.966	1.344	1.668

Table 3. Estimated uncertainties of velocities, velocity gradients, poisson's ratio and layer depths.

Model Parameter	**Uncertainty**
Depth of Layer 2A/2B boundary	±0.1 km
Depth of Layers 2/3 boundary	±0.2 km
Depth of Moho	-1.0 km to 0.8 km
Top velocity of Layer 2A	±0.2 km/s
Bottom velocity of Layer 2A	-0.3 km/s to 0.1 km/s
Velocity gradient in Layer 2A	-1.7 /s to 1.8 /s
Poisson's ratio in Layer 2A	-0.04 to 0.03
Top velocity of Layer 2B	-0.3 km/s to 0.2 km/s
Bottom velocity of Layer 2B	-0.4 km/s to 0.1 km/s
Velocity gradient in Layer 2B	-0.6 /s to 0.1 /s
Poisson's ratio in Layer 2B	-0.01 to 0.03
Top velocity of Layer 3	±0.1 km/s
Bottom velocity of Layer 3	-0.2 km/s to 0.3 km/s
Velocity gradients of Layer 3	-0.1 /s to 0.1 /s
Poisson's ratio in Layer 3	-0.01 to 0.01
Top velocity of upper mantle	-0.4 km/s to 0.1 km/s
Poisson's ratio in upper mantle	-0.01 to 0.01

Table 4. Comparison of Vp gradients (s^{-1}).

	This study						
Layer	Seg. 28	NTD	Seg. 27	mean	[1]Typical oceanic crust	[2]Mohns	[3]Serpentinite
2A	1.0	2.3	2.2	1.7	1.4	1.3-1.9	
2B	1.1	1.2	1.3	1.2		0.6-0.7	0.6-2.1
3	0.1	0.1	0.1	0.1	0.2	0.4	

1.Data from oceanic crust at age <7.5 Ma with half spreading rates in 5-20 mm/year (Christeson *et al*. 2019).

2. Data from a zero-age profile at Mohns ridge (Klingelhöfer *et al*. 2000).

3. Estimated from the compilation of Minshull (2009).

Table 5. Estimated Moho depth uncertainty.

Perturbation of bottom velocities of Layer 3	**Moho depth Uncertainty at each velocity perturbation**
+0.3 km/s	+0.8 km
+0.2 km/s	+0.6 km
+0.1 km/s	+0.4 km
-0.1 km/s	-0.9 km
-0.2 km/s	-1.0 km

Figures and captions:

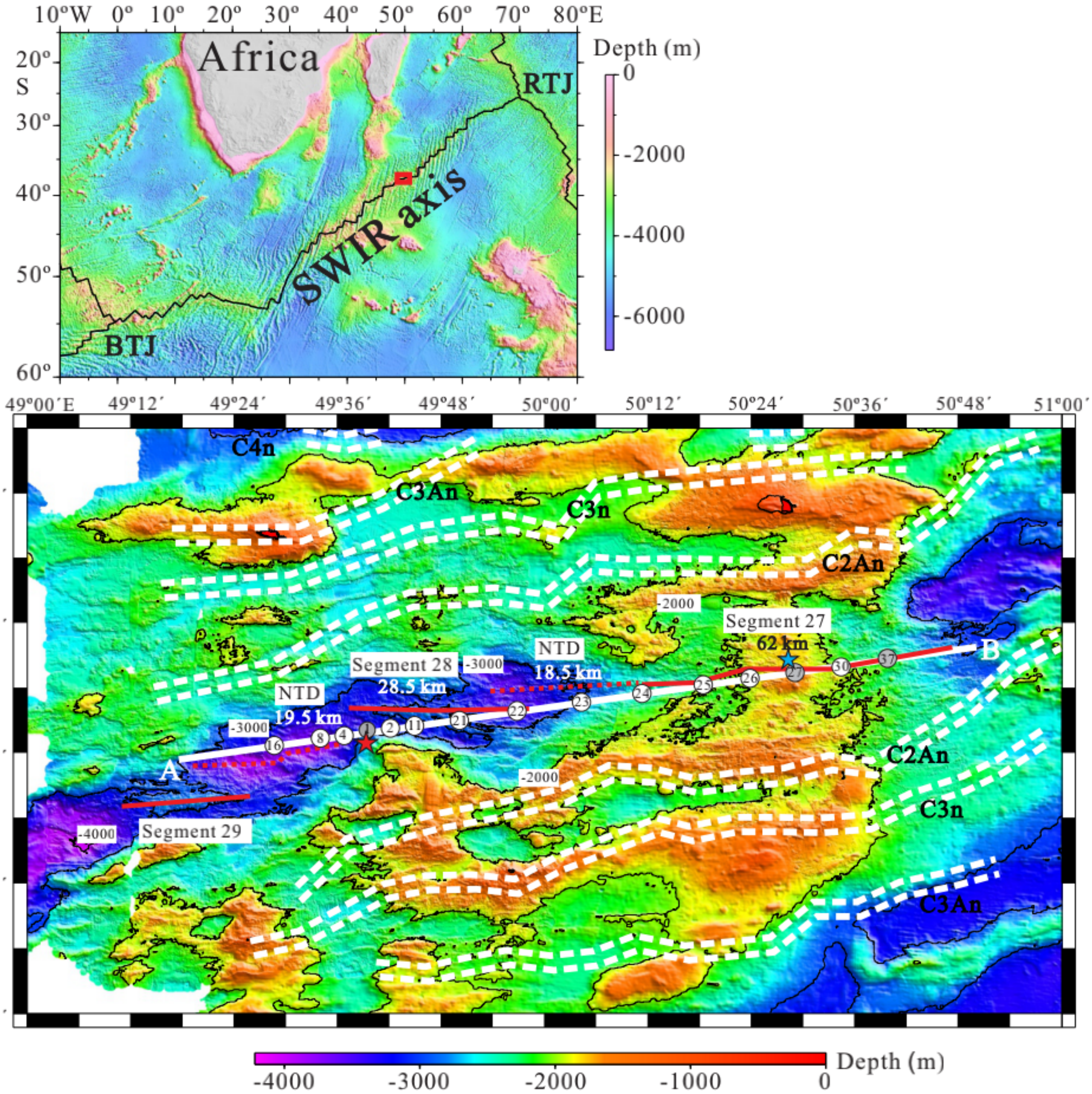

Figure 1. Bathymetry map of the research area; the data are derived from the multibeam data acquired by R/V *Dayang Yihao* and extracted from the data provided in Sauter *et al*. (2001). The solid white line indicates the seismic profile. The numbers in white circles on the line indicate the OBS stations. The red solid and dashed lines indicate the spreading segments and the NTDs, respectively (Cannat *et al*. 1999; Sauter *et al*. 2001). The red star represents the Dragon Flag active vent field discovered by the *Dayang Yihao* in 2007 (Tao *et al*. 2012). The blue star represents an inactive hydrothermal vent

(Tao *et al*. 2012). The noted double dashed white lines represent magnetic anomalies C4n (8.072 Ma), C3An (5.894 Ma), C3n (4.18 Ma), C2An (2.581 Ma), respectively (Sauter *et al*. 2009). The red rectangle in the inset shows the location of the study area. The inset shows bathymetric map of SWIR derived from ETOPO1V1. BTJ: Bouvet triple junction. RTJ: Rodriguez triple junction.

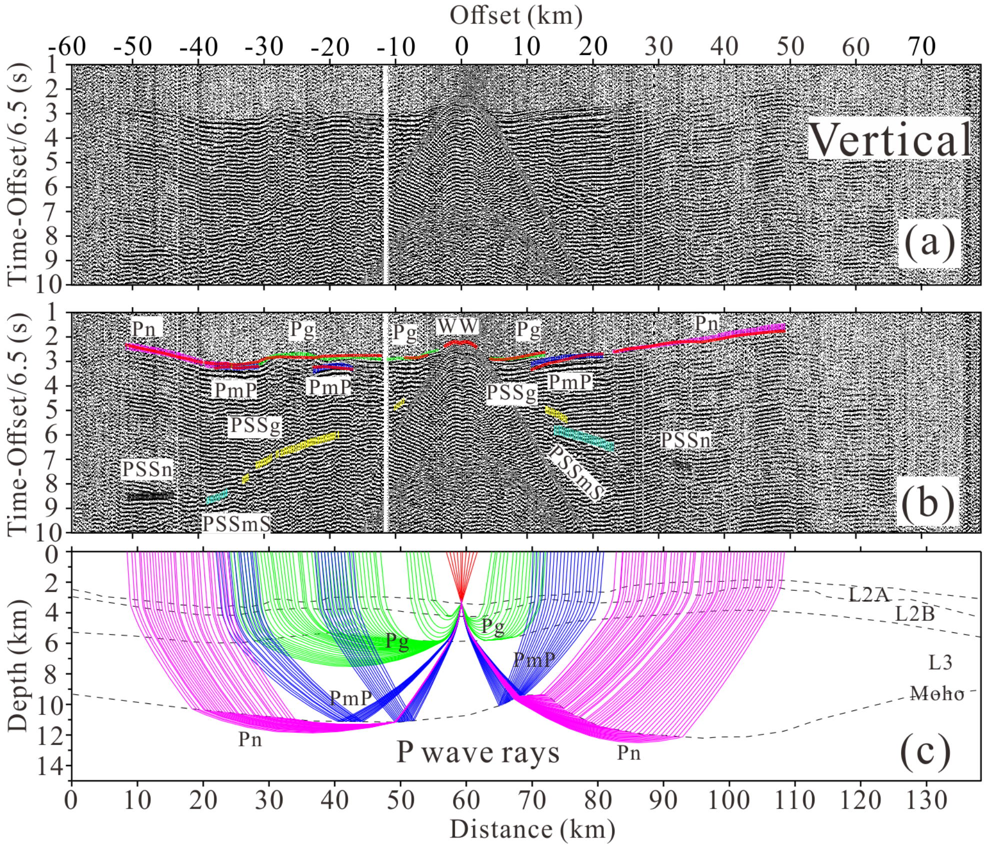

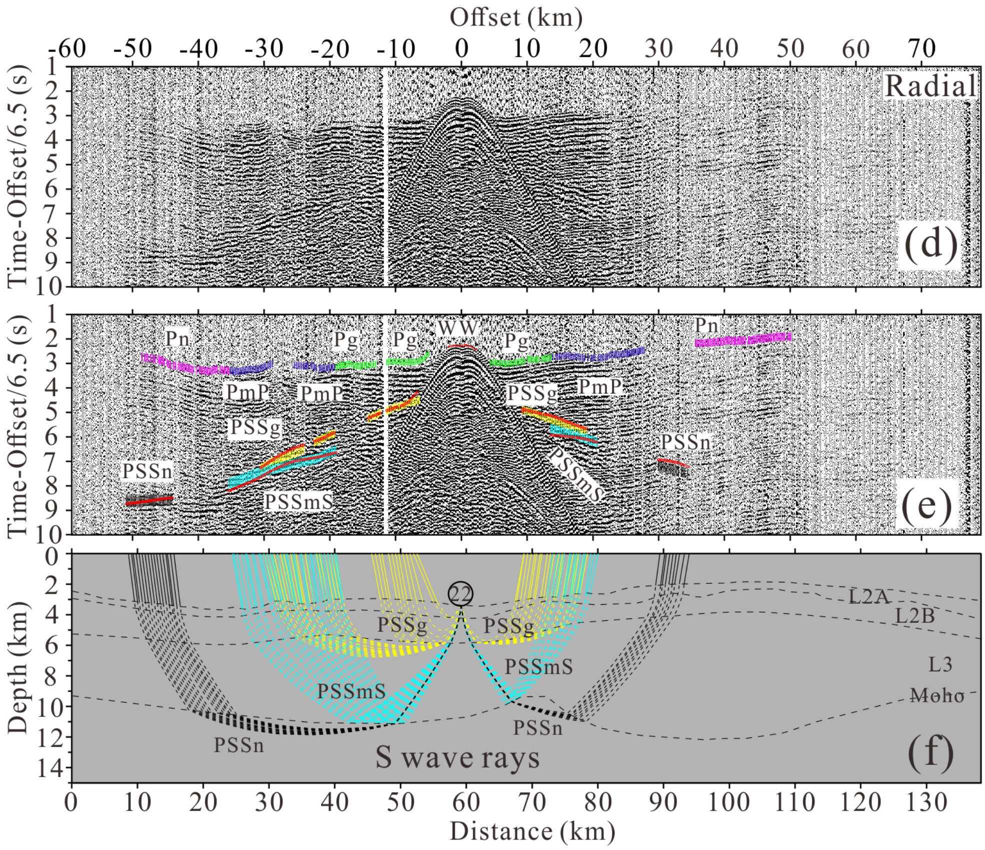

Figure 2. (a) and (d) are record sections of the vertical component and radial component of OBS 22 along profile AB, respectively. (b) and (e) are the record sections of the vertical component and radial component of OBS 22, respectively, overlain by picked and calculated travel times. (c) and (f) are the corresponding ray diagrams of the vertical component and radial component of OBS 22, respectively, with reduction velocity of 6.5 km/s. The phase labels are explained in the text. In (b) and (e), the red dots represent the predicted travel time and the colored vertical bars correspond to the rays in (c) and (f). The size of the vertical bars indicates twice the pick uncertainty (Zelt & Smith 1992). In (c), the colored lines represent P wave ray paths of different phases. In (f), the colored and black dashed lines represent S wave ray paths of different phases. In order to make the ray diagrams clearer, we only plotted one ray in every two rays. The rays were plotted

621 in 1 in 2. The layered black dashed lines from top to bottom in (c) and (f) represent the

622 seabed, the interfaces between Layer 2A and Layer 2B, Layer 2B and Layer 3, and the

623 Moho discontinuity.

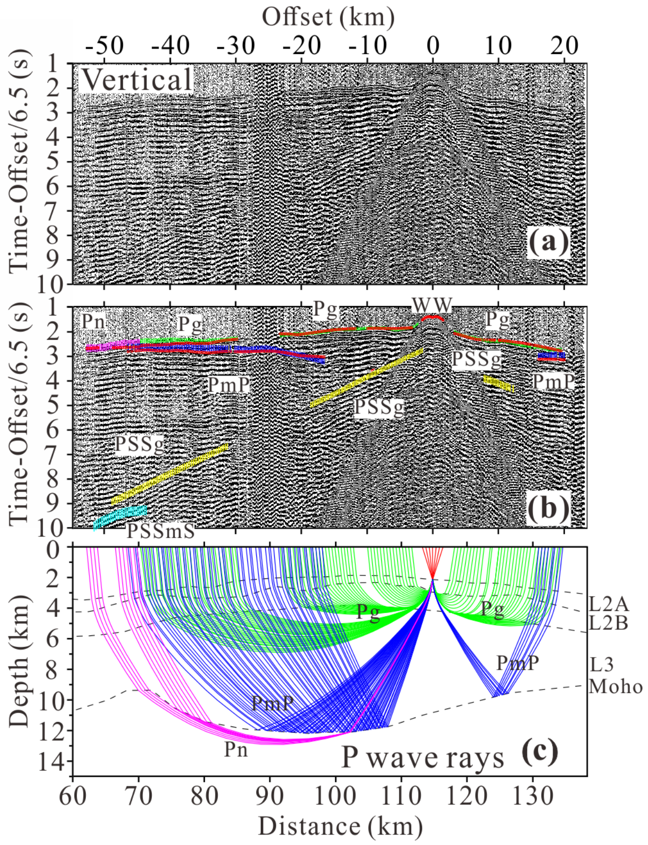

624

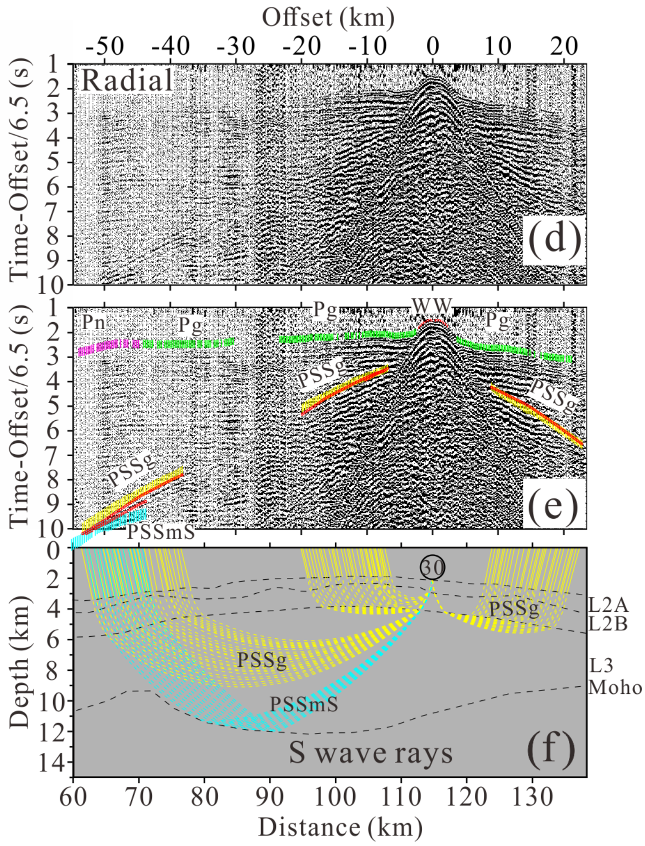

Figure 3. (a) and (d) are the record sections of the vertical component and radial component of OBS 30 along profile AB, respectively. (b) and (e) are the record sections of the vertical component and radial component of OBS 30, respectively, overlain by the picked and calculated travel-times. (c) and (f) are the corresponding ray diagrams of the vertical component and radial component of OBS 30, respectively. The other labels are the same as in Figure 2.

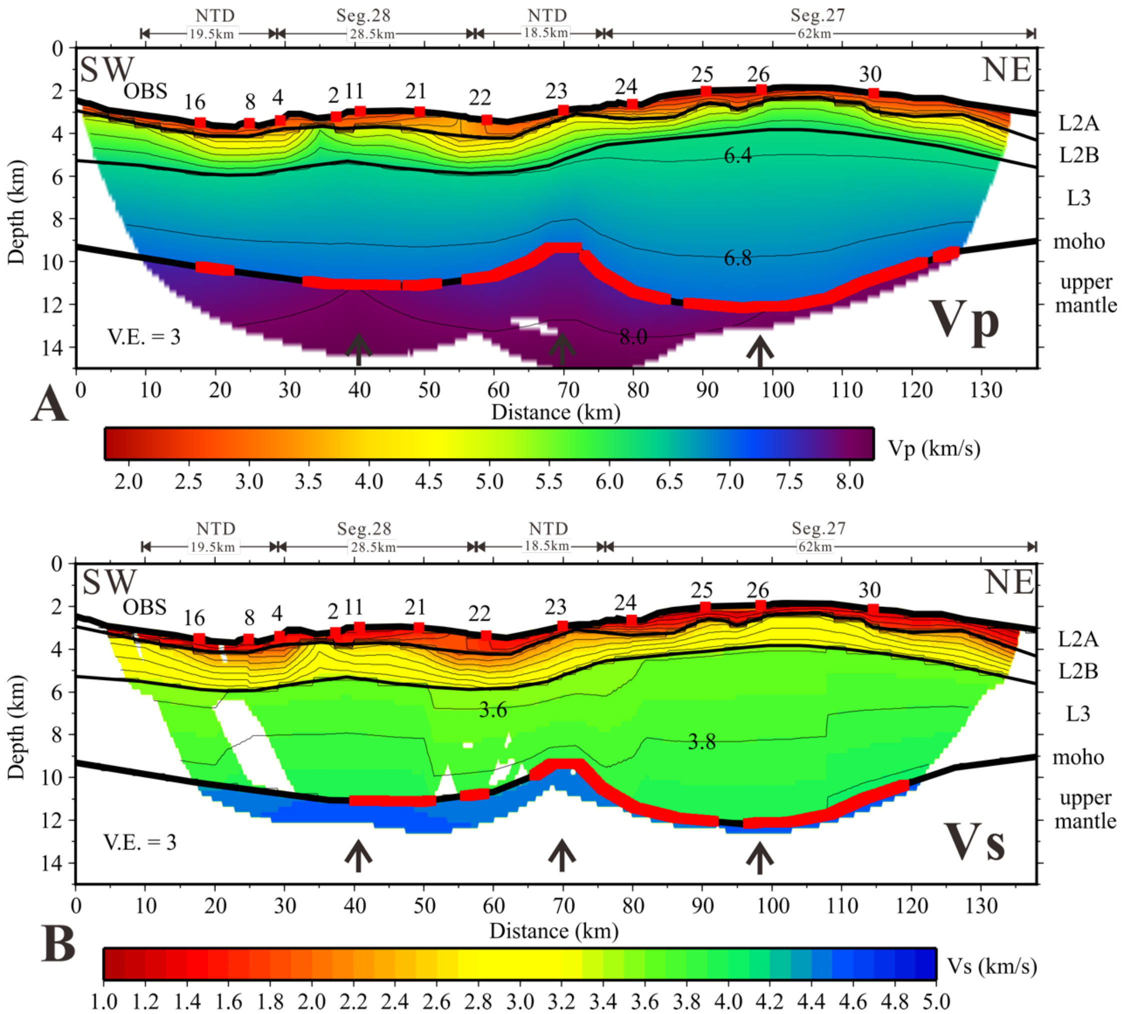

NTD 19.5km
Seg.28 28.5km
NTD 18.5km
Seg.27 62km
SW
NE
OBS
16 8 4 2 11 21 22 23 24 25 26 30
L2A
L2B
L3
moho
upper mantle
6.4
6.8
8.0
V.E. = 3
Vp
Depth (km)
Distance (km)
A
Vp (km/s)
2.0 2.5 3.0 3.5 4.0 4.5 5.0 5.5 6.0 6.5 7.0 7.5 8.0
3.6
3.8
Vs
B
Vs (km/s)
1.0 1.2 1.4 1.6 1.8 2.0 2.2 2.4 2.6 2.8 3.0 3.2 3.4 3.6 3.8 4.0 4.2 4.4 4.6 4.8 5.0

632

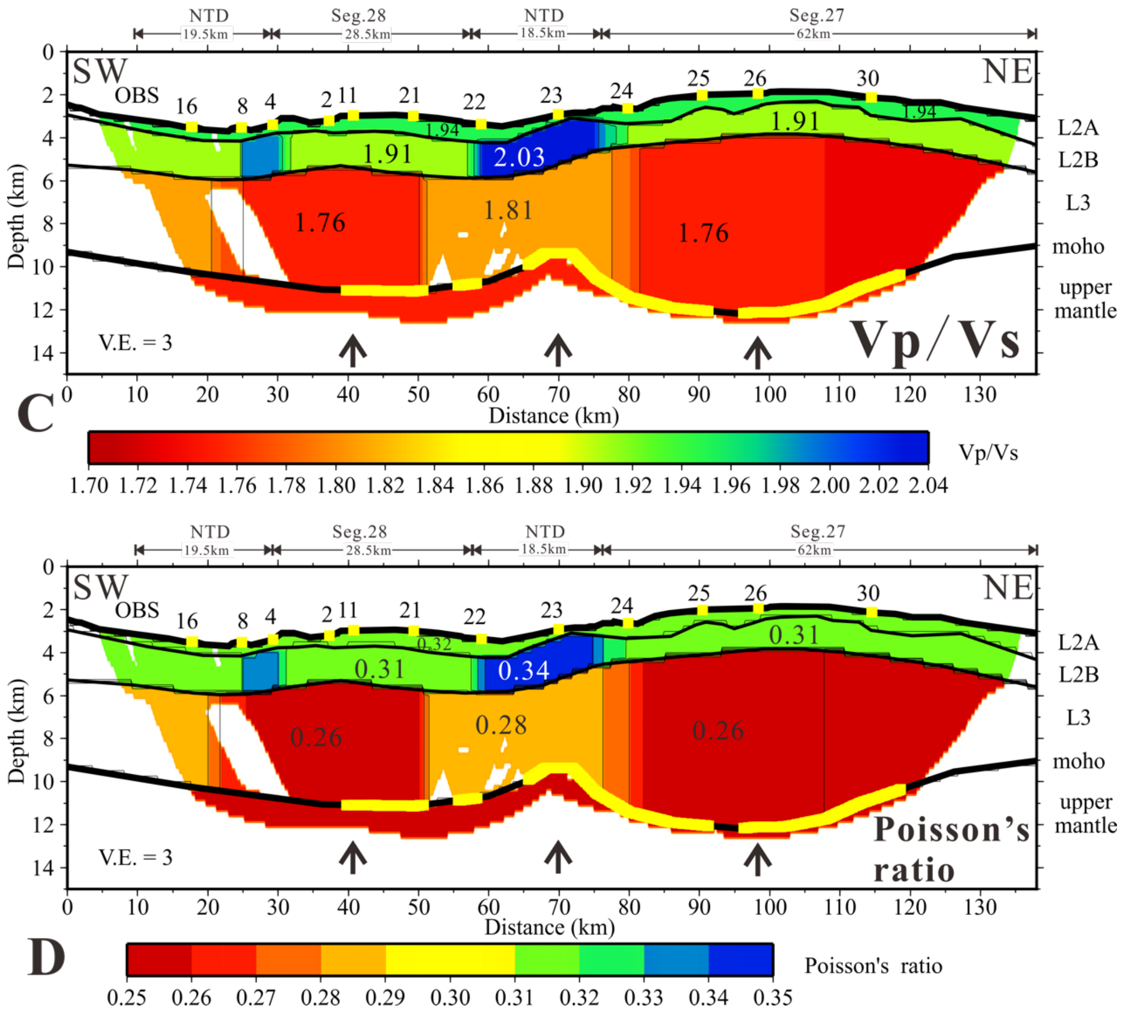

Figure 4. Models for profile AB: (a) final P-wave velocity model, with velocity contours every 0.4 km/s; (b) S-wave velocity model, with contours every 0.2 km/s; (c) Vp/Vs model, with a contour interval of 0.02; (d) Poisson's ratio model, with a contour interval of 0.01. In all four panels, numbered squares represent the OBS stations, solid black lines represent the seabed, the interface between oceanic layers 2A and 2B, the interface between oceanic layers 2B and 3, and the Moho discontinuity, respectively; black arrows at the bottom show the locations of the 1-D models shown in Figure 5 (labelled in (a) and (b) with crustal thickness). In (a) and (b), the red colored portion of the Moho marks sections constrained by PmP and PSSmS reflections, respectively. The yellow areas of

the Moho in (c) and (d) mark sections constrained by PSSmS reflections. The vertical exaggeration is 3.

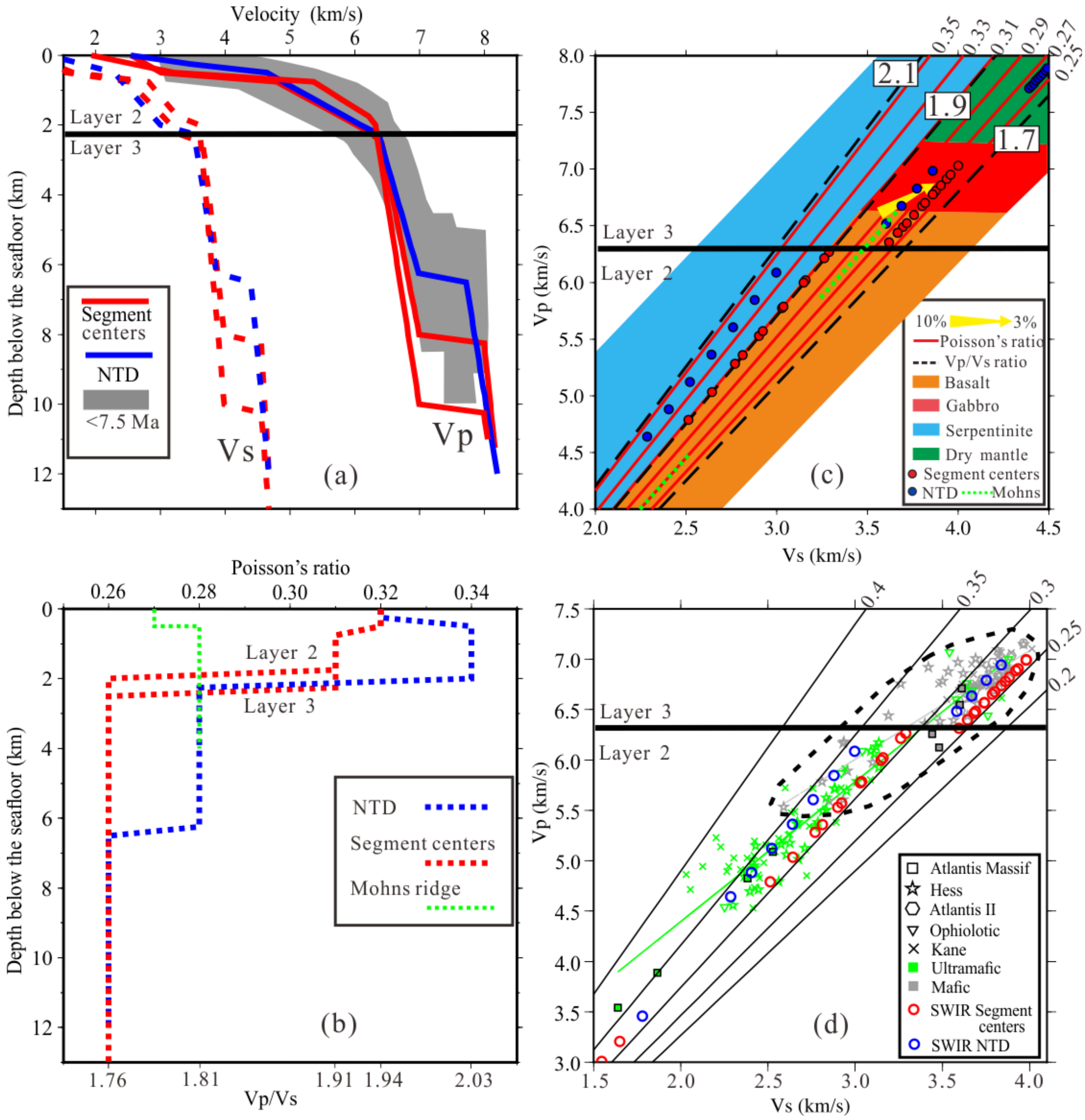

Figure 5. (a) 1-D velocity–depth variations sampled from segments 27 and 28 (segment centeres) and NTD (black arrows in Figure 4). The red and blue solid lines represent the P-wave velocity from Layer 2B and Layer 3 in the segment centres and NTD, respectively, while the dashed red and blue lines represent the S-wave velocity from the segment centres and NTD, respectively. The gray shaded envelope bounds velocities for ridge of age of 0–7.5 Ma with half spreading rate of 5–20 mm/year

(Christeson *et al*. 2019). (b) Vp/Vs and Poisson's ratio (dashed lines) structures compared with previous study. The blue and red lines represent the Vp/Vs and Poisson's ratio structures beneath the NTD, segment centeres, respectively. The green lines represent the Poisson's ratio beneath Mohns ridge (Klingelhöfer *et al*. 2000). (c) Vp/Vs as a proxy for rock types and mantle serpentinisation. The black dashed lines with numbers in the panel indicate the Vp/Vs values. The rock type field defiitions are from Grevemeyer *et al*. (2018). The filled red and blue circles represent data beneath segment centres and the NTD, respectively. The red lines with labels on the top right of the chart represent the Poisson's ratio calculated in this study. The head and tail of the yellow arrow represent, respectively, the result of adding 3% and 10% melt to a gabbro with a Vp of 7.0 km/s and a Vs of 4.0 km/s. The dotted green lines represent Poisson's ratio of zero-age crust at Mohns ridge (Klingelhöfer *et al*. 2000). (d) Comparison between Vp and Vs of Layer 3 beneath the NTD and segment centres at SWIR with the mafic and ultramafic samples under the confining pressure of 50 MPa (Bayrakci *et al*. 2018). The open red and blue circles represent data beneath segment centres and the NTD, respectively. Squares represent data from Atlantis Massif (Blackman *et al*. 2006; Früh-Green *et al*. 2017); crosses represent data from Kane transform fault (Miller & Christensen 1997); stars represent data from Hess Deep (Iturrino *et al*. 1996); diamonds represent data from Atlantis II fracture zone (Iturrino *et al*. 1991); and inverted triangles represent data from ophiolitic partially serpentinised peridotites (Christensen 1966). Thin black lines represent Poisson's ratios. Gray and green lines represent the least squares curves for Vp/Vs of ultramafic and mafic samples, respectively. In panels (a), (c) and (d), the thick black line marks the boundary between Layer 2 and Layer 3 of our models.

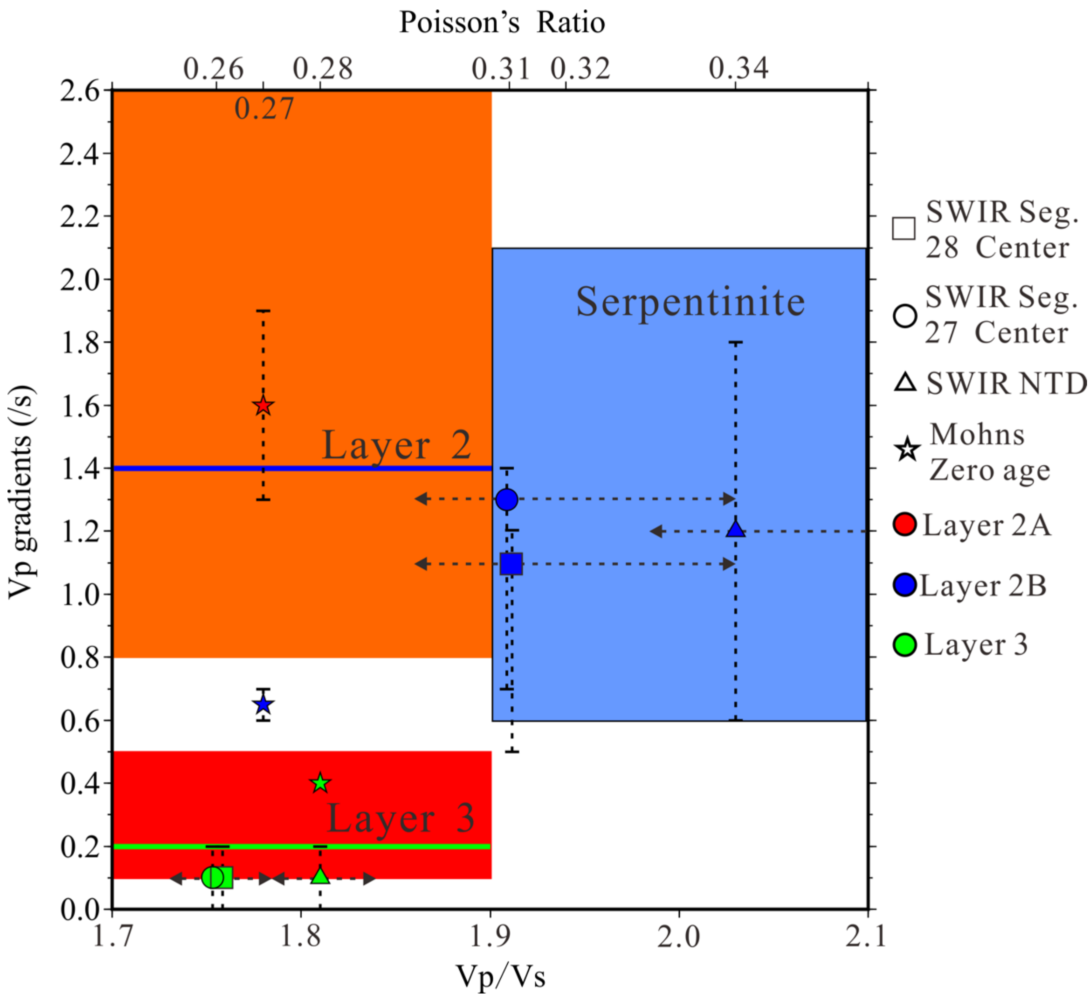

Figure 6. Distinguishing lithology based on Vp/Vs ratio and Vp gradients. Rectangles, circles, triangles and stars represent data from segment center 27, segment center 28, the NTD between them and zero-age crust at Mohns Ridge (Klingelhöfer *et al*. 2000), respectively. Layer 2A data are omitted because their Vp gradients have large uncertainties. The blue and green colours represent data from Layer 2B and Layer 3, respectively. The dashed lines crossing the symbols with bars or triangles at their ends represent the Vp gradients and Poisson's ratio errors, respectively. In order to make error bars visible when Vp/Vs values are the same, we made small adjusments to these values. The blue line and orange region represent respectively the mean and standard deviation of Layer 2 velocity gradients for < 7.5 Ma oceanic crust with half-spreading

rates in 5-20 mm/year (Christeson *et al*. 2019). The green line and red region mark the corresponding values for Layer 3. The blue region marks serpentinite, with Vp/Vs ≥ 1.9 (Grevemeyer *et al*. 2018) and Vp gradients of 0.6 /s~2.1 /s (see text).

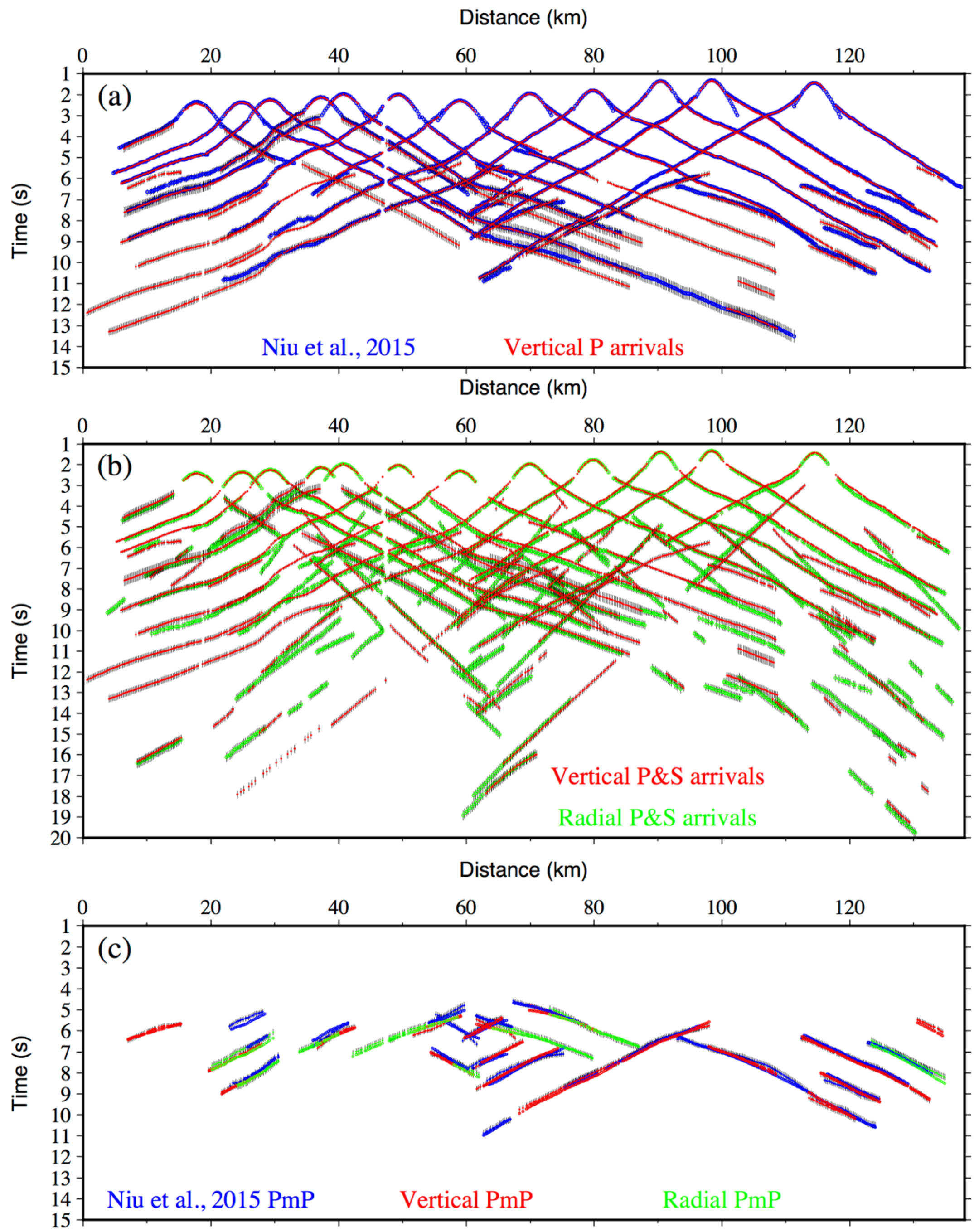

Figure S1. Pick arrivals comparison. (a) P wave picks from Niu *et al*. 2015 (blue) and from vertical components of this study (red), with error bars for both shown in black. Note that a significant number of new picks have been added. (b) P and S wave picks from picked in vertical (red) and radial (green) components, with their error bars (black). (c) Calculated PmP arrivals and picked PmP arrivals for this study and Niu *et* *al*. (2015). The red and green dots with black error bars represent PmP arrivals picked from vertical and radial components, respectively. The red and green circles represent calculated PmP arrivals in this study. The red and green circles fit the PmP arrivals picked from vertical and radial component, respectively. The blue dots with black error bars and blue circles denote PmP arrivals picked and calculated PmP arrivals in Niu *et al*. (2015).

Fig.S2

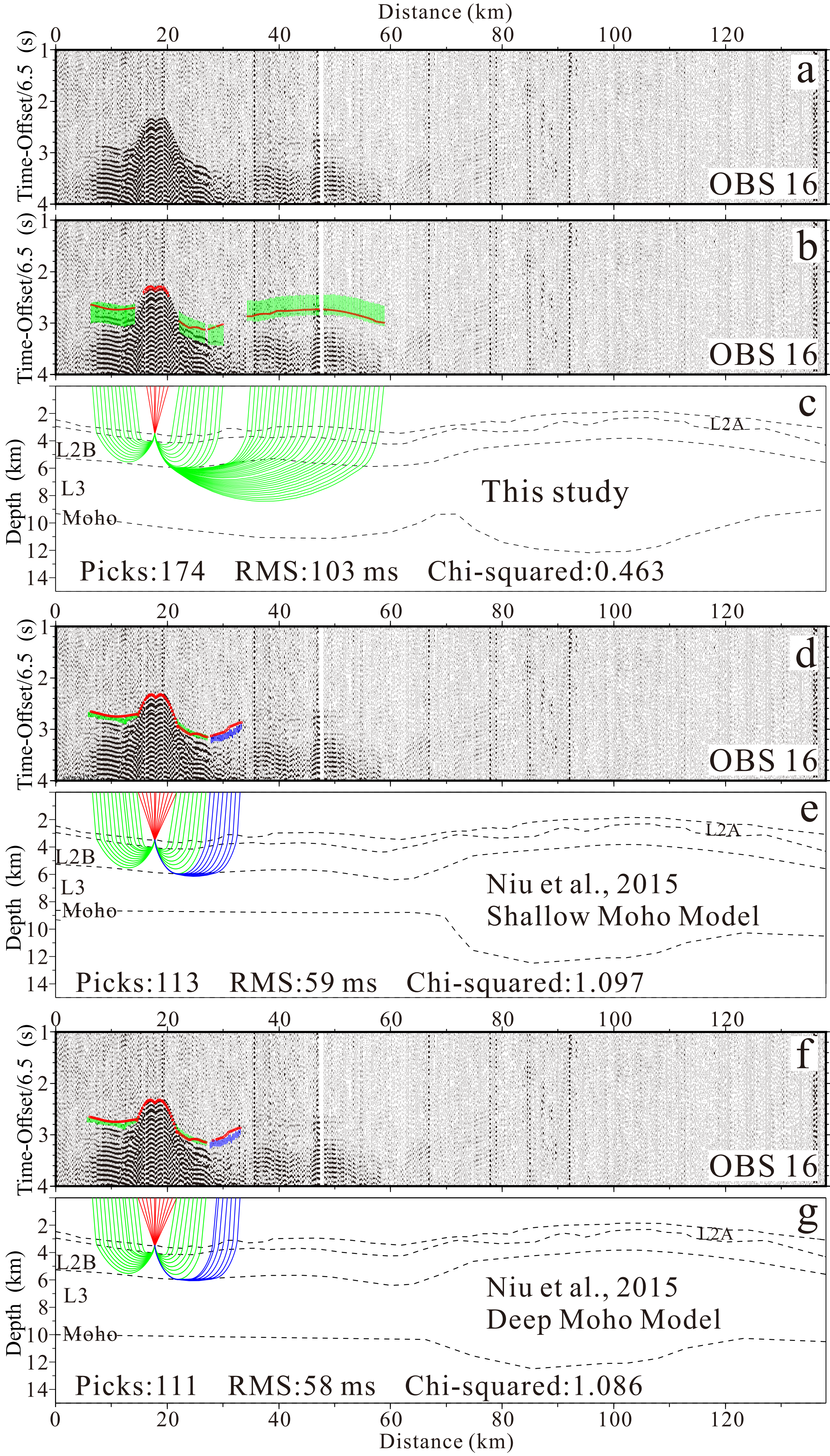

Distance (km)
0 20 40 60 80 100 120
Time-Offset/6.5 (s)
a
OBS 16
b
OBS 16
c
Depth (km)
L2A
L2B
L3
Moho
This study
Picks:174 RMS:103 ms Chi-squared:0.463
d
OBS 16
e
Niu et al., 2015
Shallow Moho Model
Picks:113 RMS:59 ms Chi-squared:1.097
f
OBS 16
g
Niu et al., 2015
Deep Moho Model
Picks:111 RMS:58 ms Chi-squared:1.086

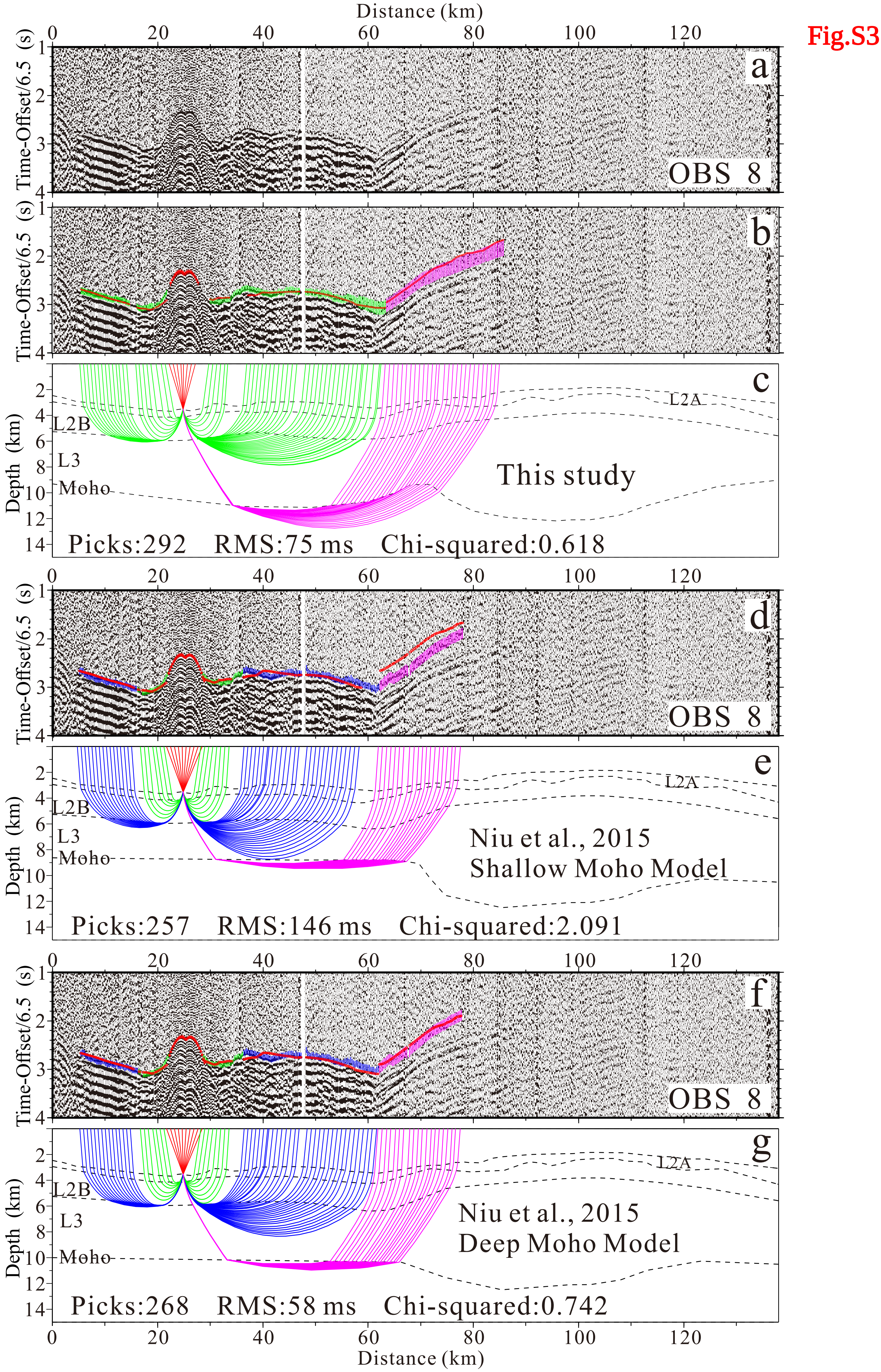
Fig.S3
Distance (km)
Time-Offset/6.5 (s)
Depth (km)
a
b
c
d
e
f
g
OBS 8
L2A
L2B
L3
Moho
This study
Picks:292 RMS:75 ms Chi-squared:0.618
Niu et al., 2015
Shallow Moho Model
Picks:257 RMS:146 ms Chi-squared:2.091
Niu et al., 2015
Deep Moho Model
Picks:268 RMS:58 ms Chi-squared:0.742

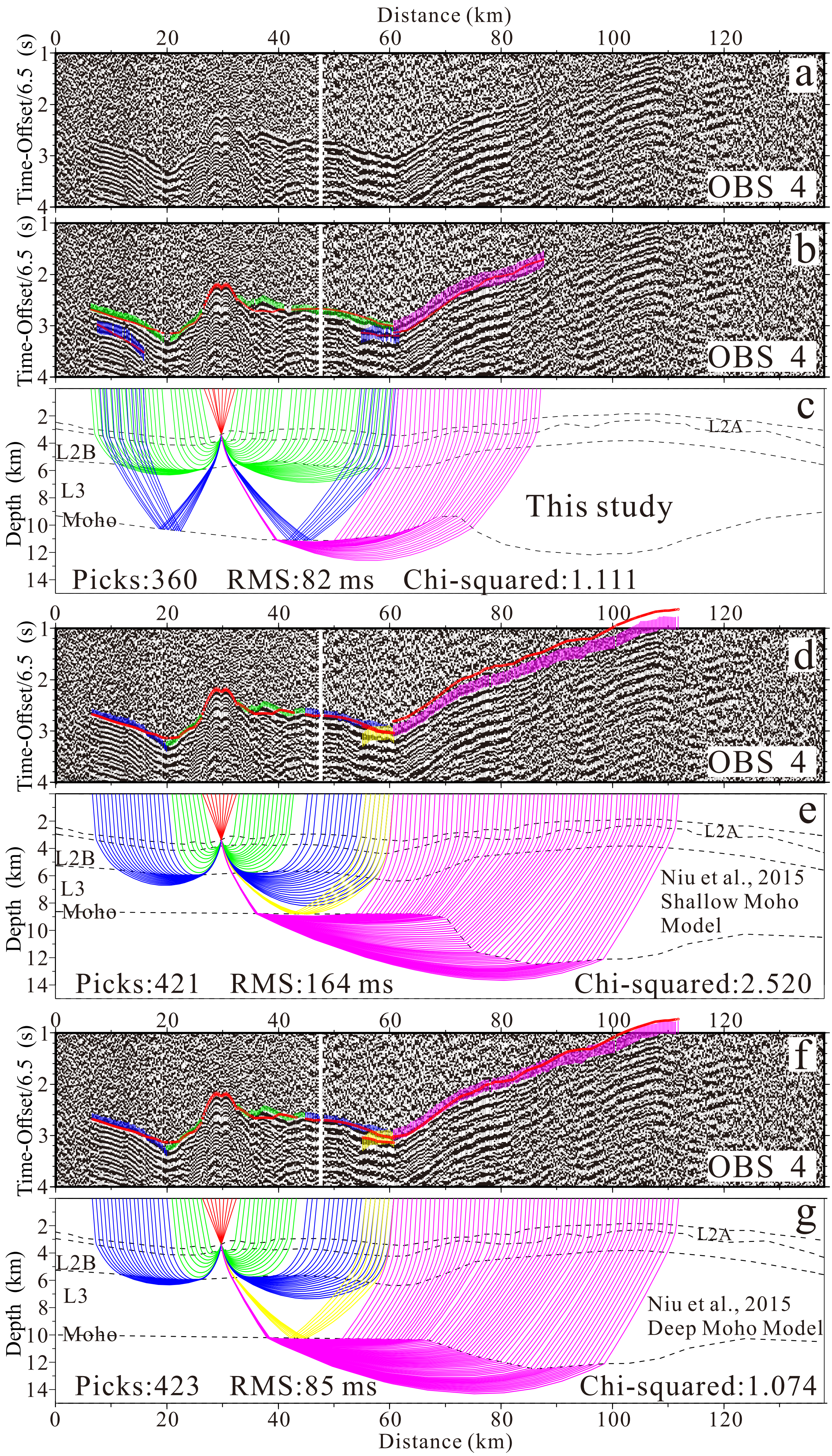

Distance (km)
a
b
c
d
e
f
g
OBS 4
Time-Offset/6.5 (s)
Depth (km)
L2A
L2B
L3
Moho
This study
Picks:360 RMS:82 ms Chi-squared:1.111
Niu et al., 2015
Shallow Moho
Model
Picks:421 RMS:164 ms Chi-squared:2.520
Niu et al., 2015
Deep Moho Model
Picks:423 RMS:85 ms Chi-squared:1.074

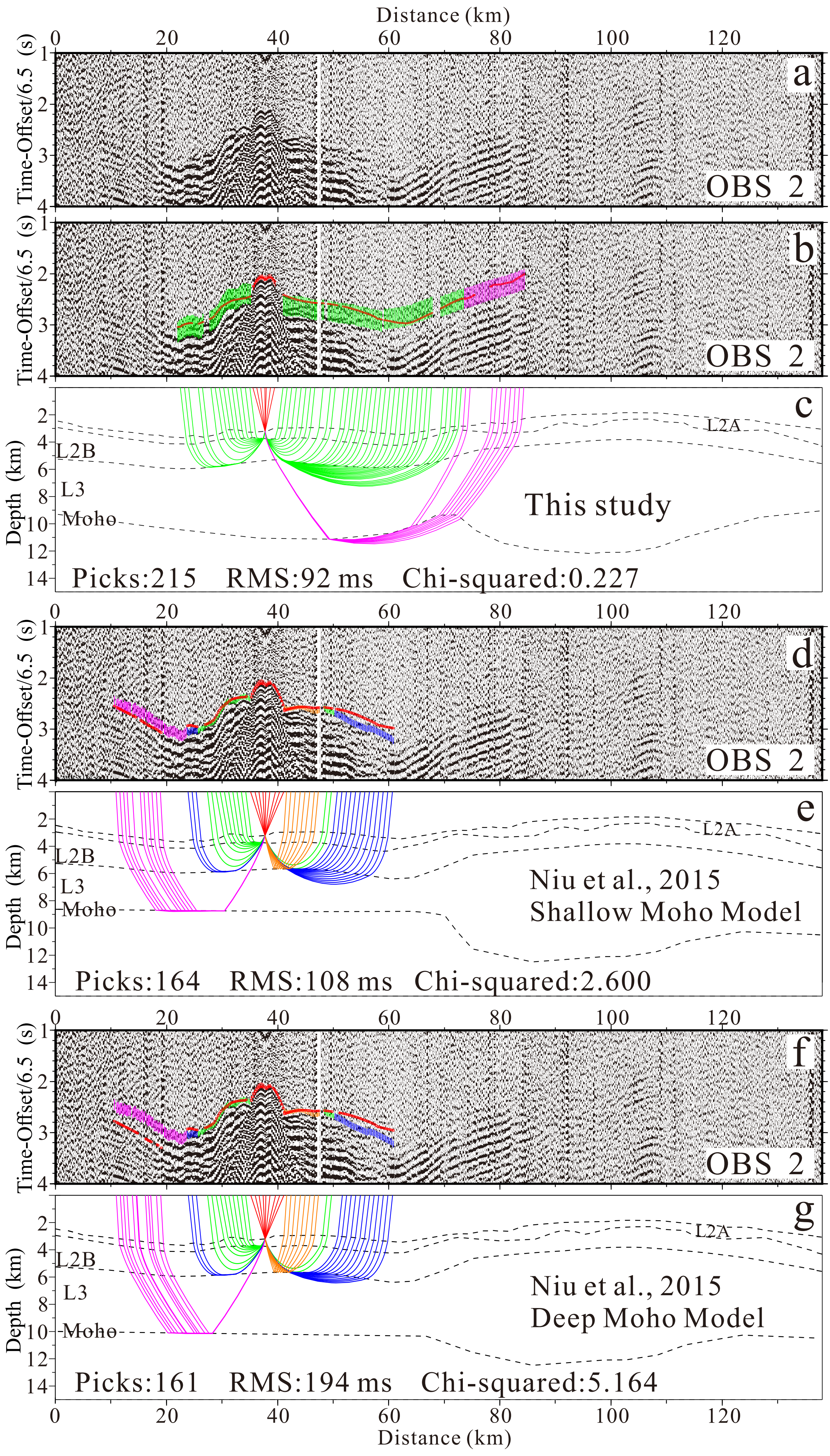

Distance (km)
a
b
c
d
e
f
g
OBS 2
Time-Offset/6.5 (s)
Depth (km)
L2A
L2B
L3
Moho
This study
Picks:215 RMS:92 ms Chi-squared:0.227
Niu et al., 2015
Shallow Moho Model
Picks:164 RMS:108 ms Chi-squared:2.600
Niu et al., 2015
Deep Moho Model
Picks:161 RMS:194 ms Chi-squared:5.164

Fig.S6

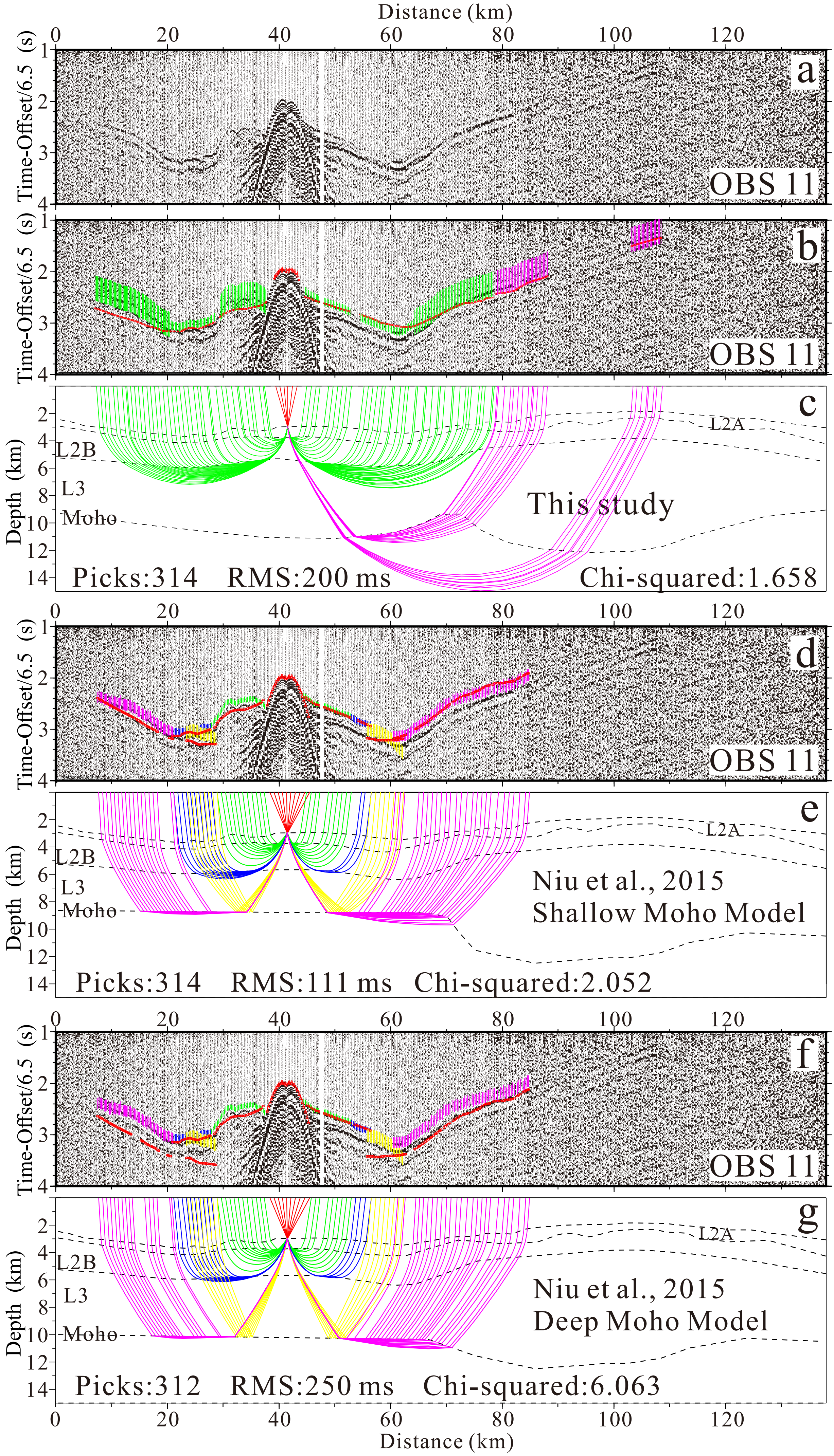

Distance (km)
0 20 40 60 80 100 120
Time-Offset/6.5 (s)
a
OBS 11
b
OBS 11
c
Depth (km)
L2A
L2B
L3
Moho
This study
Picks:314 RMS:200 ms Chi-squared:1.658
d
OBS 11
e
Niu et al., 2015
Shallow Moho Model
Picks:314 RMS:111 ms Chi-squared:2.052
f
OBS 11
g
Niu et al., 2015
Deep Moho Model
Picks:312 RMS:250 ms Chi-squared:6.063

Fig.S7

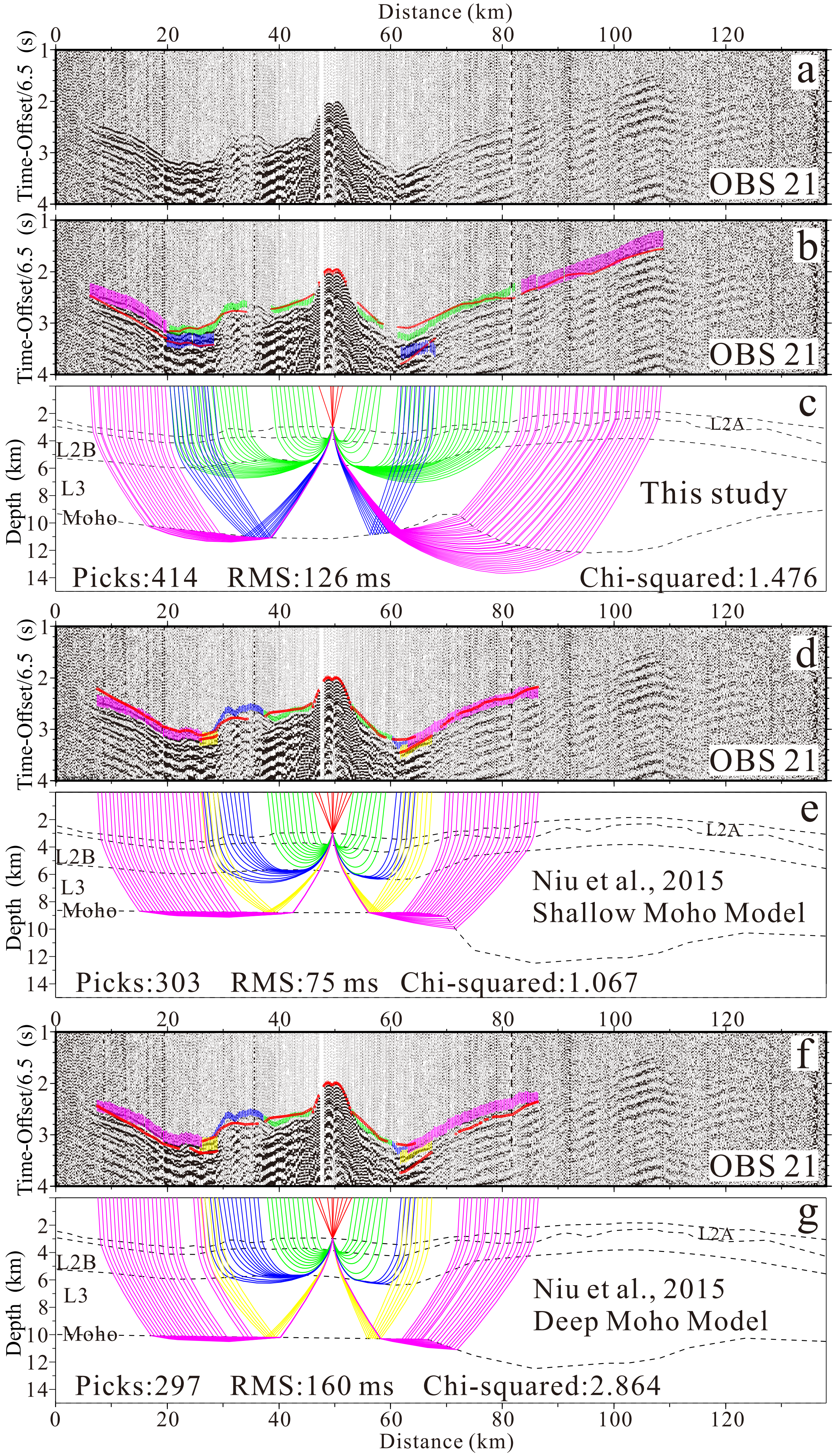

Distance (km)
a
OBS 21
b
OBS 21
c
L2A
L2B
L3
Moho
This study
Picks:414 RMS:126 ms Chi-squared:1.476
d
OBS 21
e
L2A
L2B
L3
Moho
Niu et al., 2015
Shallow Moho Model
Picks:303 RMS:75 ms Chi-squared:1.067
f
OBS 21
g
L2A
L2B
L3
Moho
Niu et al., 2015
Deep Moho Model
Picks:297 RMS:160 ms Chi-squared:2.864
Time-Offset/6.5 (s)
Depth (km)
Distance (km)

Fig.S8

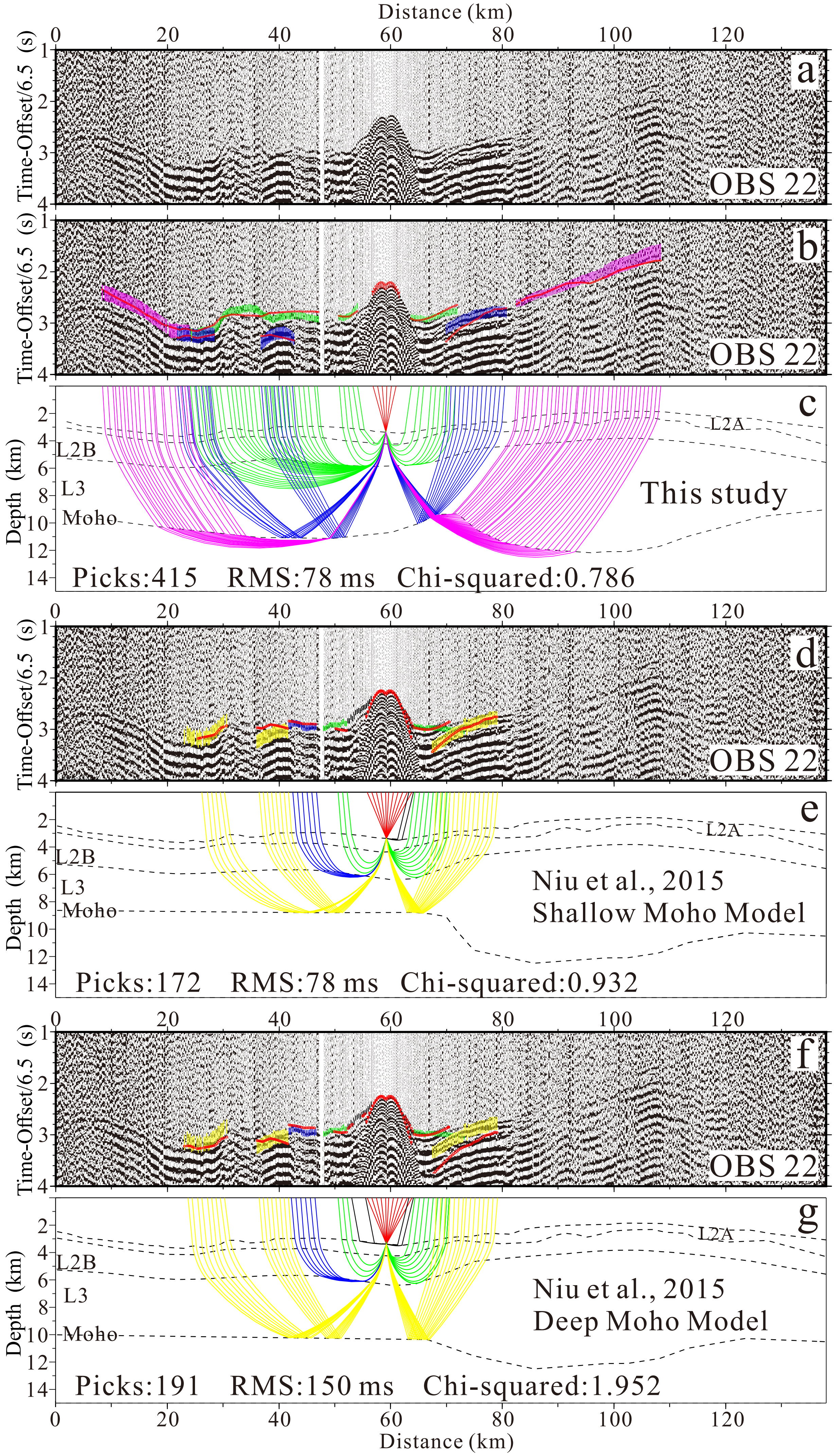

Distance (km)
Time-Offset/6.5 (s)
a
OBS 22
b
OBS 22
c
Depth (km)
L2A
L2B
L3
Moho
This study
Picks:415 RMS:78 ms Chi-squared:0.786
d
OBS 22
e
L2A
L2B
L3
Moho
Niu et al., 2015
Shallow Moho Model
Picks:172 RMS:78 ms Chi-squared:0.932
f
OBS 22
g
L2A
L2B
L3
Moho
Niu et al., 2015
Deep Moho Model
Picks:191 RMS:150 ms Chi-squared:1.952
Distance (km)

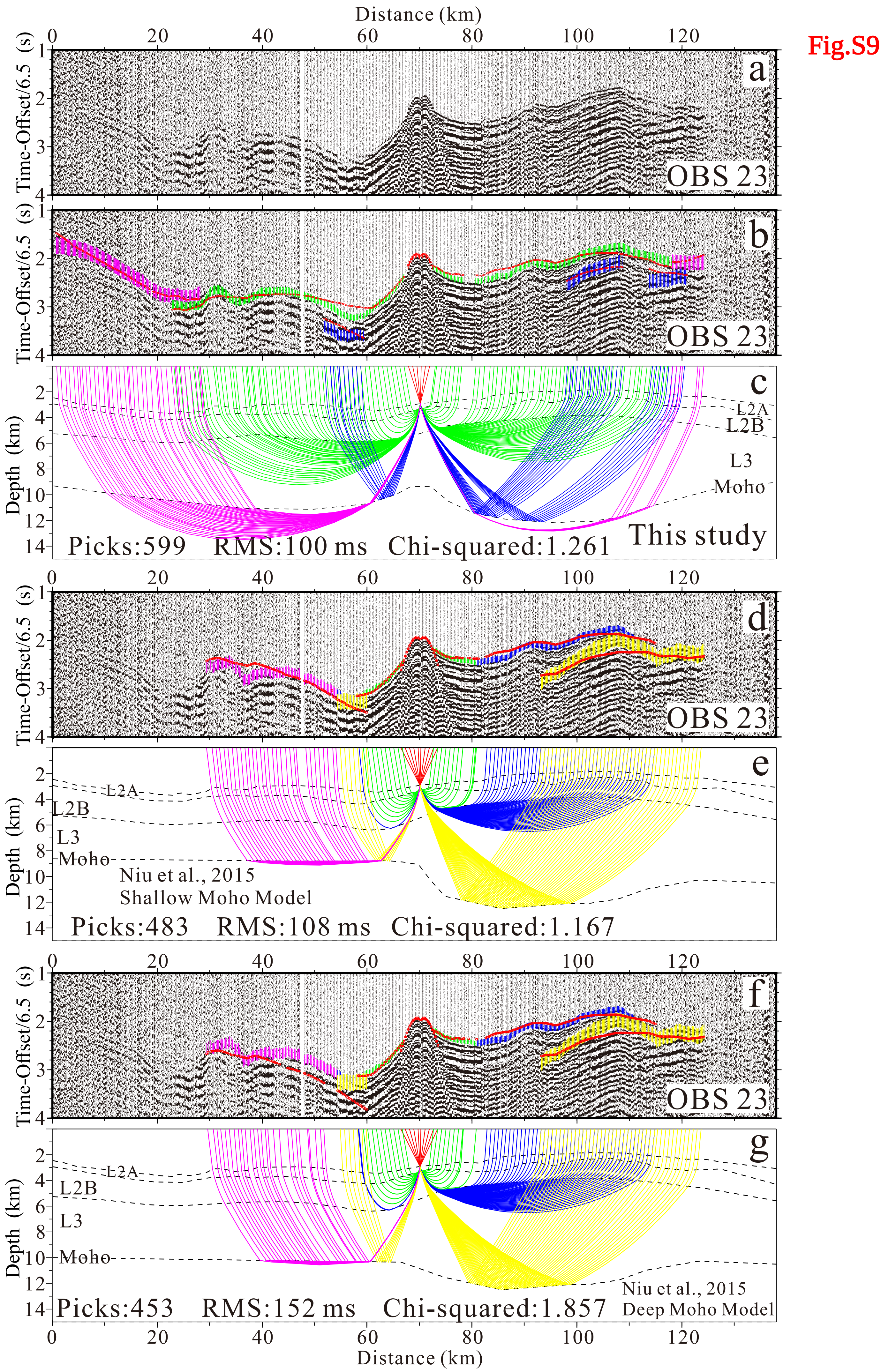

Fig.S9
Distance (km)
Time-Offset/6.5 (s)
Depth (km)
a
b
c
d
e
f
g
OBS 23
L2A
L2B
L3
Moho
Picks:599 RMS:100 ms Chi-squared:1.261
This study
Niu et al., 2015
Shallow Moho Model
Picks:483 RMS:108 ms Chi-squared:1.167
Picks:453 RMS:152 ms Chi-squared:1.857
Niu et al., 2015
Deep Moho Model

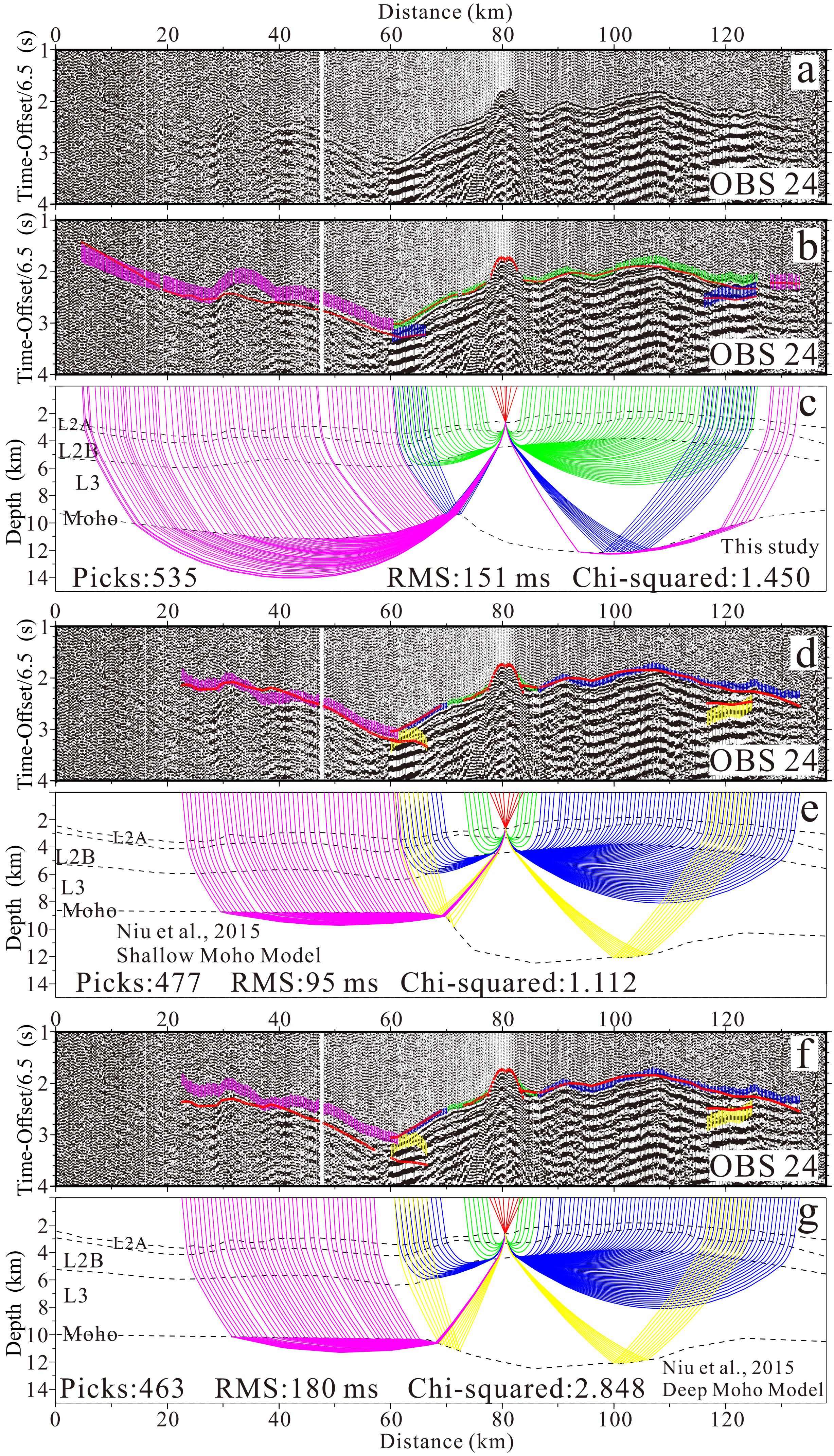
Distance (km)
0
20
40
60
80
100
120
Time-Offset/6.5 (s)
1
2
3
4
a
OBS 24
b
OBS 24
c
Depth (km)
2
4
6
8
10
12
14
L2A
L2B
L3
Moho
This study
Picks:535
RMS:151 ms
Chi-squared:1.450
d
OBS 24
e
L2A
L2B
L3
Moho
Niu et al., 2015
Shallow Moho Model
Picks:477
RMS:95 ms
Chi-squared:1.112
f
OBS 24
g
L2A
L2B
L3
Moho
Niu et al., 2015
Deep Moho Model
Picks:463
RMS:180 ms
Chi-squared:2.848
Distance (km)

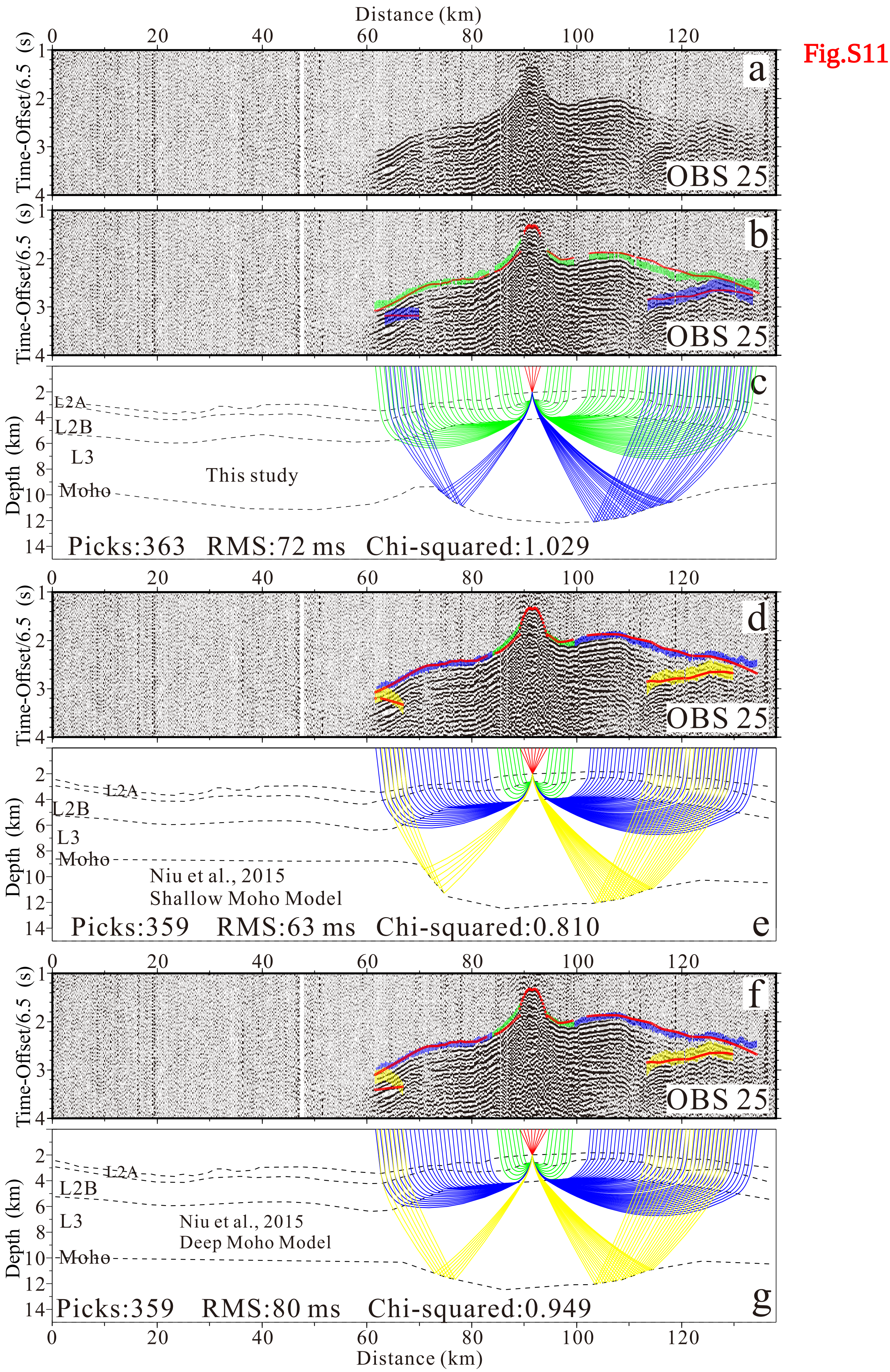

Fig.S11
Distance (km)
Time-Offset/6.5 (s)
OBS 25
a
b
c
d
e
f
g
L2A
L2B
L3
Moho
Depth (km)
This study
Picks:363 RMS:72 ms Chi-squared:1.029
Niu et al., 2015
Shallow Moho Model
Picks:359 RMS:63 ms Chi-squared:0.810
Niu et al., 2015
Deep Moho Model
Picks:359 RMS:80 ms Chi-squared:0.949

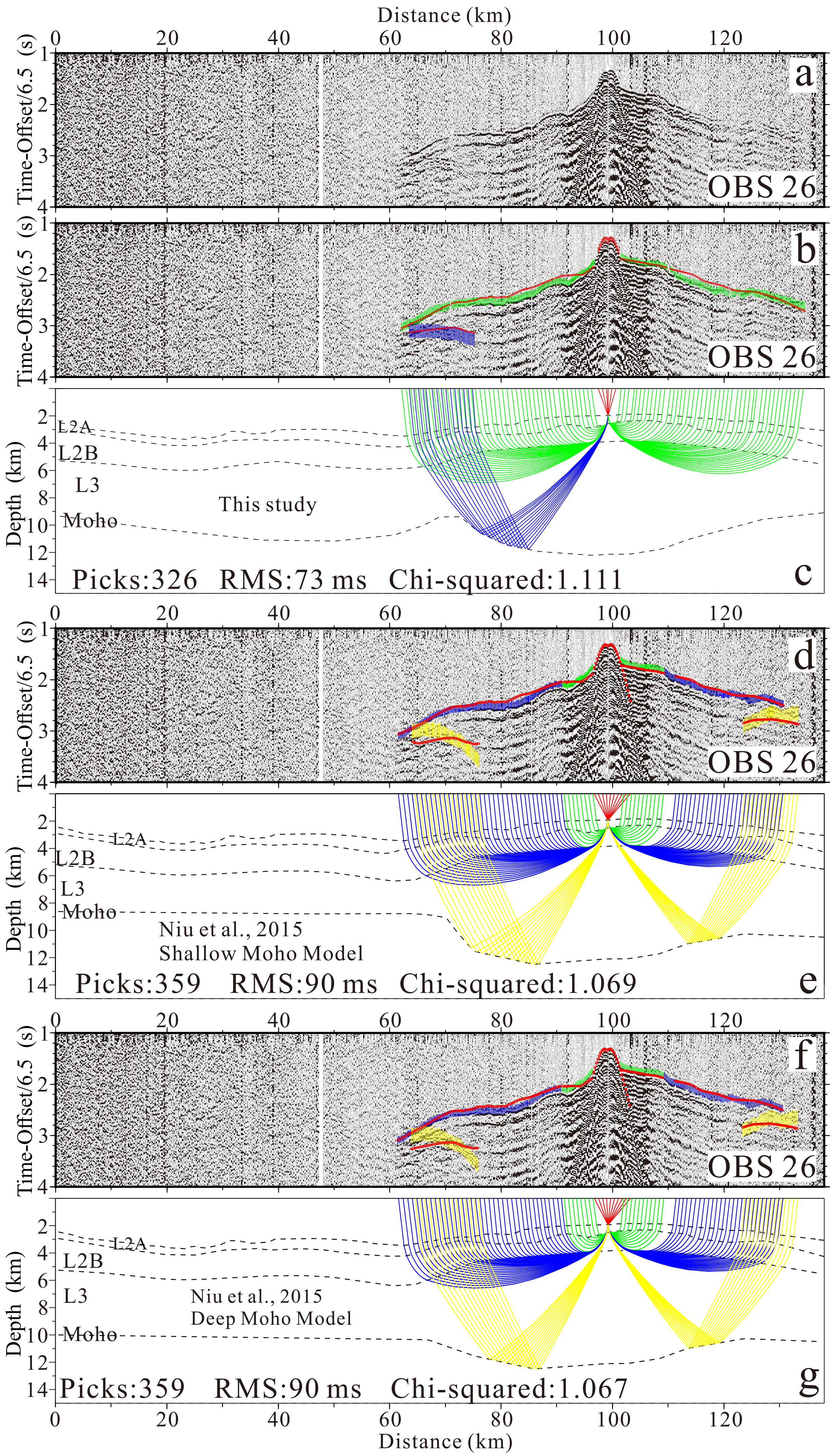
Distance (km)
0 20 40 60 80 100 120
Time-Offset/6.5 (s)
a
OBS 26
b
OBS 26
Depth (km)
L2A
L2B
L3
Moho
This study
Picks:326 RMS:73 ms Chi-squared:1.111
c
d
OBS 26
L2A
L2B
L3
Moho
Niu et al., 2015
Shallow Moho Model
Picks:359 RMS:90 ms Chi-squared:1.069
e
f
OBS 26
L2A
L2B
L3
Moho
Niu et al., 2015
Deep Moho Model
Picks:359 RMS:90 ms Chi-squared:1.067
g
Distance (km)

Fig.S13

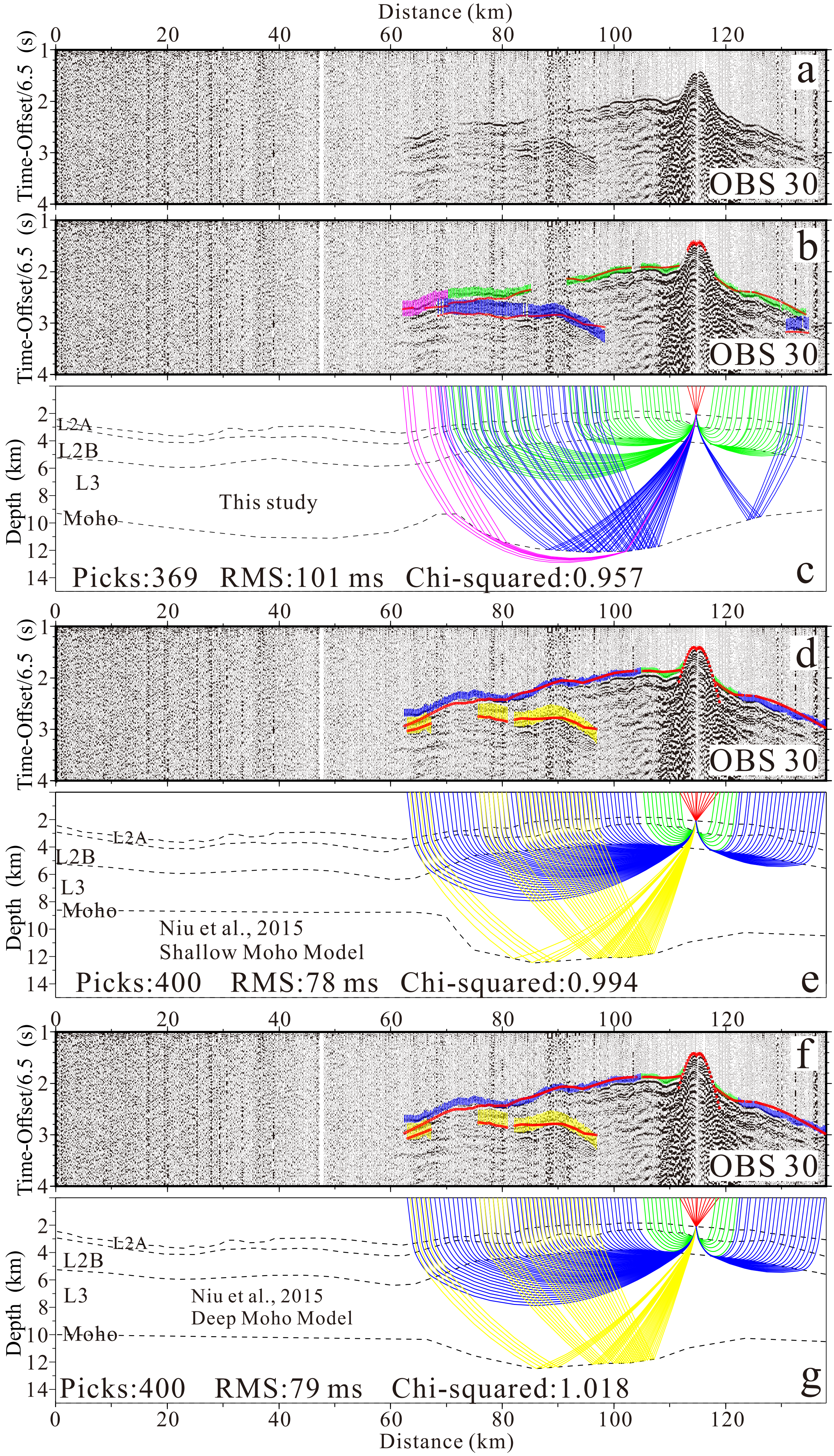

Distance (km)
0
20
40
60
80
100
120
Time-Offset/6.5 (s)
a
OBS 30
b
OBS 30
Depth (km)
L2A
L2B
L3
Moho
This study
Picks:369 RMS:101 ms Chi-squared:0.957
c
d
OBS 30
L2A
L2B
L3
Moho
Niu et al., 2015
Shallow Moho Model
Picks:400 RMS:78 ms Chi-squared:0.994
e
f
OBS 30
L2A
L2B
L3
Moho
Niu et al., 2015
Deep Moho Model
Picks:400 RMS:79 ms Chi-squared:1.018
g

Figure S2.(a) Vertical component data from OBS16. (b) Travel-time fit and (c) corresponding ray-tracing for this study. (d)-(e) and (f)-(g) Travel-time fit and raytracing for Niu et al.'s (2015) shallow and deep Moho models, respectively. In panels (b), (d) and (f), the coloured bars represent picked arrivals with error bars, while the red circles represent calculated arrival times for the model. The corresponding umber of picks, RMS traveltime residual (RMS) and normalized chi-squared are also shown. The dashed lines in panels (c), (e) and (g) mark the seabed, the Layer 2A/2B boundary, the Layer 2B/3 boundary and the Moho. The reduction velocity is 6.5 km/s. In order to make the ray diagrams clearer, we only plotted one ray in every three rays.

Figure S3. The same as Figure S2 but for OBS8.

Figure S4. The same as Figure S2 but for OBS4.

Figure S5. The same as Figure S2 but for OBS2.

Figure S6. The same as Figure S2 but for OBS11.

Figure S7. The same as Figure S2 but for OBS21.

Figure S8. The same as Figure S2 but for OBS22.

Figure S9. The same as Figure S2 but for OBS23.

Figure S10. The same as Figure S2 but for OBS24.

Figure S11. The same as Figure S2 but for OBS25.

Figure S12. The same as Figure S2 but for OBS26.

Figure S13. The same as Figure S2 but for OBS30.

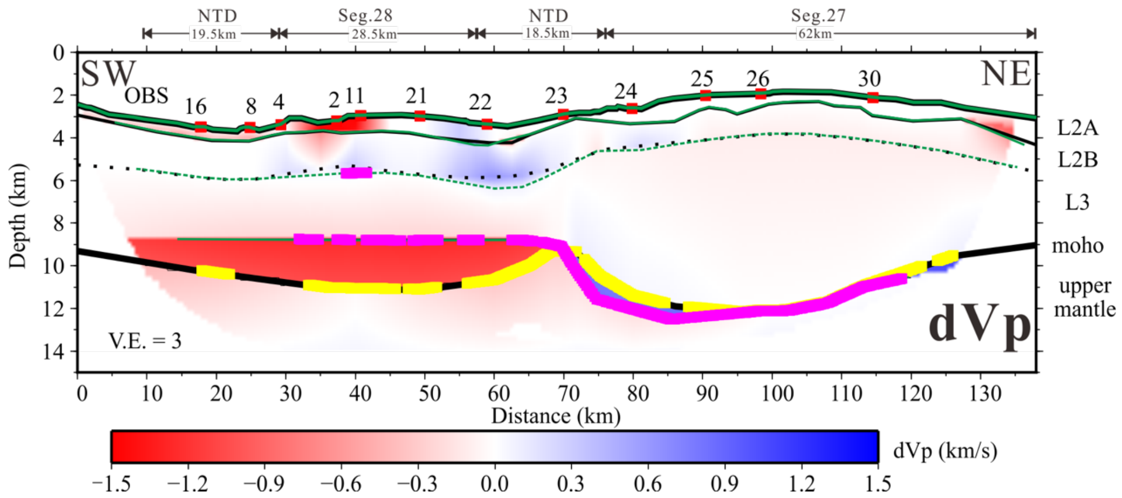

Figure S14. Difference between our Vp model and that shallow Moho version of Niu *et al*. (2015). The green solid and dashed lines represent the layer boundaries of the Vp model of Niu *et al*. (2015), while the black solid and dashed lines represent our new layer boundaries. The thick pink and yellow lines represent the reflection points of Niu *et al*.'s (2015) Vp model and our new model, respectively.

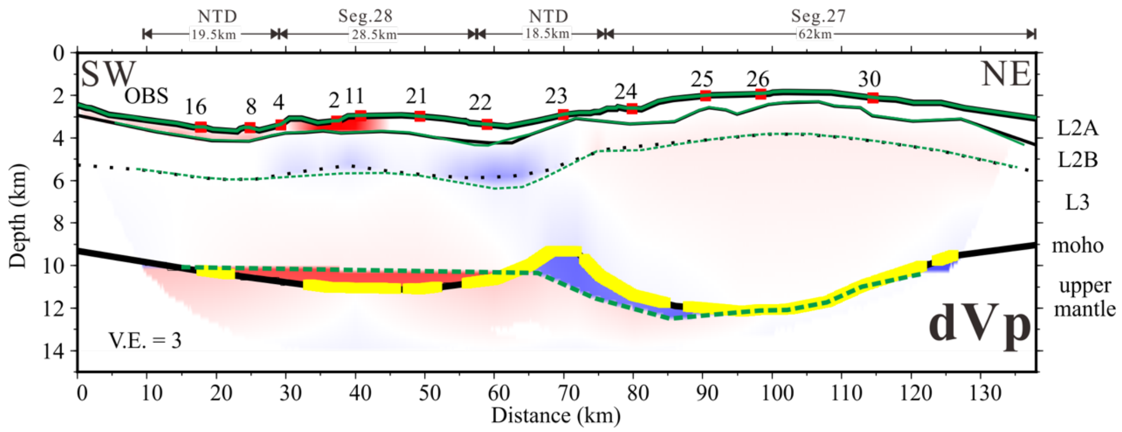

Figure S15. Difference between our Vp model and that deep Moho of Niu *et al*. (2015). The green solid and dashed lines represent the layer boundaries of the Vp model of Niu *et al*. (2015), while the black solid and dashed lines represent our new layer boundaries. The thick yellow lines represent the reflection points of our new model. Colour contouring is as for Figure S14.

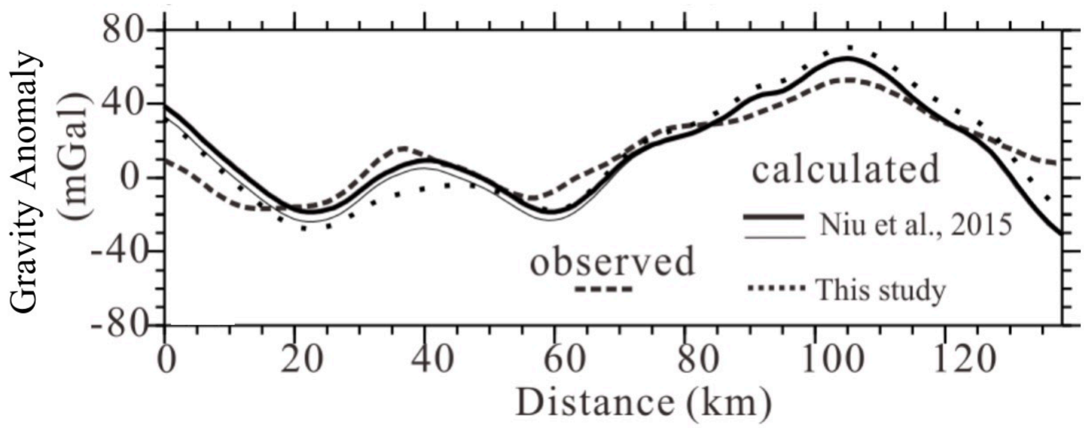

Figure S16. Gravity anomaly along the profile. Dashed line marks satellite-derived gravity anomaly. Dotted line marks the gravity anomaly calculated for a model in which seismic velocity model in this study is converted to density. Thick and thinner solid lines marks the calculated anomaly corresponding to the seismic velocity model of Niu *et al*. (2015). The density values are calculated by using a velocity and density relationship of ρ=3.81-6.0/Vp (Carlson & Herrick, 1990).

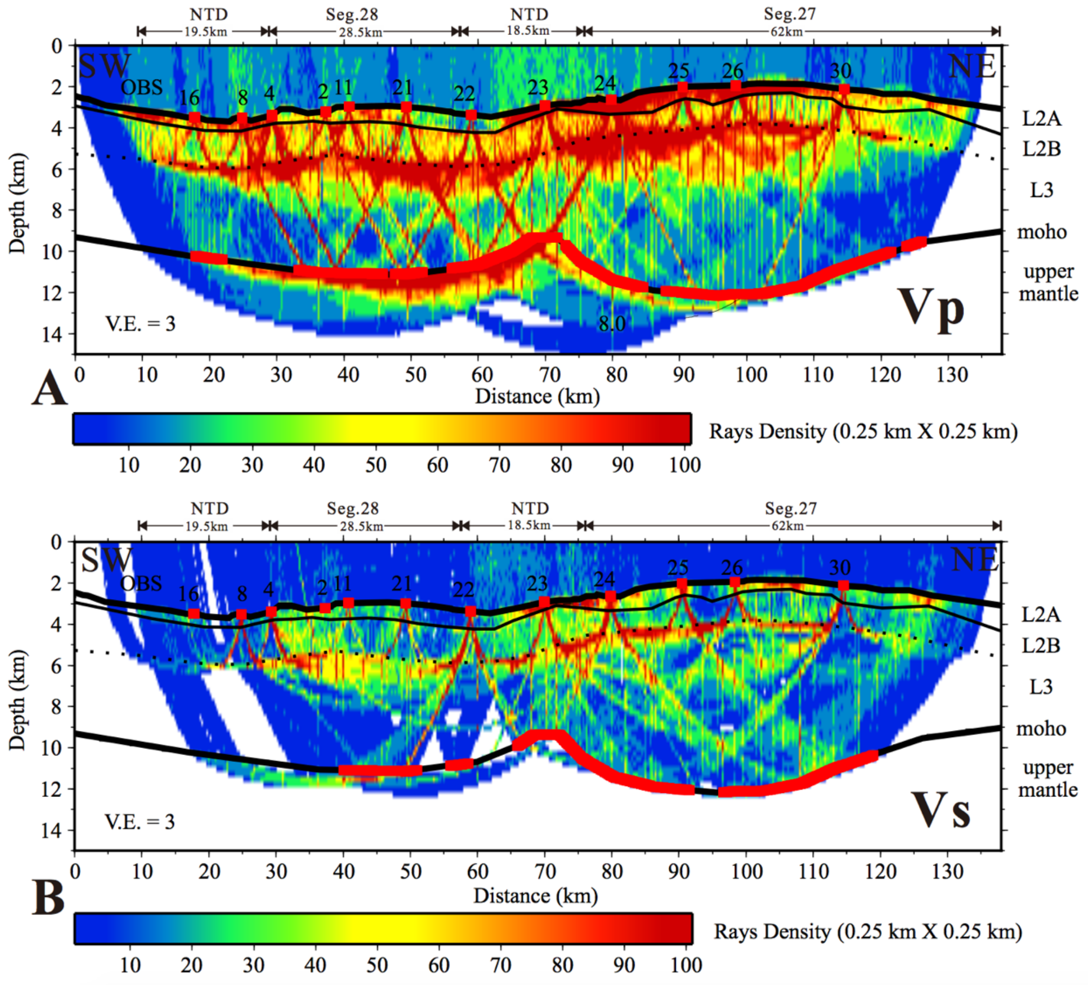

Figure S17. Ray density for Vp model (A) and Vs model (B) in 0.25 × 0.25 km cells. The other labels are the same as in Fig. 4.